A Spectroscopic Compton Scattering Reconstruction Algorithm for 2D Cross-Sectional View of Breast CT Geometry

by

Tamar Chighvinadze

A Thesis submitted to the Faculty of Graduate Studies of

The University of Manitoba

in partial fulfillment of the requirement of the degree of

MASTER OF SCIENCE

Department of Physics and Astronomy

University of Manitoba

Winnipeg, Manitoba

ABSTRACT

X-ray imaging exams are widely used procedures in medical diagnosis. Whenever an x-ray imaging procedure is performed, it is accompanied by scattered radiation. Scatter is a significant contributor to the degradation of image quality in breast CT. This work uses our understanding of the physics of Compton scattering to overcome the reduction in image quality that typically results from scattered radiation. By measuring the energy of the scattered photons at various locations about the object, an electron density (ρ_e) image of the object can be obtained.

This work investigates a system modeled using a 2D cross-sectional view of a breast CT geometry. The ρ_e images can be obtained using filtered backprojection over isogonic curves. If the detector has ideal energy and spatial resolution, a single projection will enable a high quality image to be reconstructed. However, these ideal characteristics cannot be achieved in practice and as the detector size and energy resolution diverge from the ideal, the image quality degrades. To compensate for the realistic detector specifications a multi-projection Compton scatter tomography (MPCST) approach was introduced. In this approach an x-ray source and an array of energy sensitive photon counting detectors located just outside the edge of the incident fan-beam, rotate around the object while acquiring scattering data. The ρ_e image quality is affected by the size of the detector, the energy resolution of the detector and the number of projections. These parameters, their tradeoffs and the methods for the image quality improvement were investigated.

The work has shown that increasing the energy and spatial resolution of the detector improves the spatial resolution of the reconstructed ρ_e image. These changes in the size and energy resolution result in an increase in the noise. Thus optimizing the image quality becomes a tradeoff between blurring and noise. We established that a suitable balance is achieved with a 500 eV energy resolution and 2×2 mm^2 detector. We have also established that using a multi-projection approach can offset the increase in the noise.

ACKNOWLEGEMENTS

TABLE OF CONTENTS

LIST OF FIGURES AND TABLES

LIST OF ABBREVIATIONS

CT	Computed tomography
CST	Compton scatter tomography
MPCST	Multi-projection Compton scatter tomography
FT	Fourier transform
FBP	Filtered backprojection
MTF	Modulation transfer function
PSNR	Peak signal-to-noise ratio
CNR	Contrast-to-noise ratio
LSF	Line spread function
MSE	Mean square error
ROI	Region of interest
PSF	Point spread function
SPR	Scatter-to-primary ratio

CHAPTER 1. Introduction and Rationale

Cancer is a common disease hallmarked by uncontrolled, abnormal cell growth. As the disease progresses the uncontrolled cell growth spreads to the surrounding tissues, organs and through the body. The various types of cancer are classified by the origin of abnormal cell growth, such as breast cancer, which originates in the breast tissue at its early stage before spreading to surrounding tissues in later stages.

Breast cancer is the most common type of cancer among women worldwide, with 1.7 million cases diagnosed, and 522,000 deaths caused by this disease in 2012 [5, 6]. Early detection is vital given that the five year survival rate increases from 23% to 99% when breast cancer is diagnosed at the localized stage vs. when it is detected after the cancer has spread [7].

The universally accepted standard for breast cancer screening is an x-ray imaging procedure called mammography. During this procedure, an image of a compressed breast is acquired from two nearly orthogonal views and is recorded on film or on digital, flat panel, media. This imaging technique has been proven to decrease the mortality rate due to breast cancer; however the benefit vs. harm ratio continues to be controversial [8-10]. A common outcome of this procedure involves a number of false positive/negative diagnoses leading to over/under treatment [11]. A key issue associated with this breast imaging modality is that the 3D structure is projected onto a 2D plane. Thus, the imaging of the small low contrast lesions embedded in the normal breast formation is difficult.

In computed tomography (CT), the image is created from data acquired from many projections. Consequently, the image obtained using this approach has depth perception in the axial plane of the imaged object. This image characterizes the distribution of the x-ray attenuation coefficient within the imaged object [1]. After its introduction in the early 1970's, CT technology quickly developed. It evolved from a first generation system, where a pencil beam of x-rays

performed scanning and translation motion, to a fourth generation system which uses stationary ring detectors. The third generation CT, where the source and detectors revolve around the object to be imaged is the most widely utilized [12, 13].

Soon after the conception of CT, dedicated breast CT was introduced. While it was considered a useful tool for imaging the breast, its limited spatial resolution and higher dose, relative to conventional mammography, put the advancement of this imaging modality on hold for several decades [14]. Recent development in detector technology has reignited interest in breast CT [15-17]. Currently, a number of research projects are devoted to the investigation of this modality [14, 18, 19]. Dedicated breast CT addresses the problem associated with planar imaging such as mammography by providing volumetric information. It produces images under a dose constraint that is similar to the one used in mammography. A clinical study evaluating dedicated breast CT indicates that when it comes to the imaging of the breast lesions, the performance of this imaging modality is comparable to that of mammography. It outperforms mammography for visualization of masses, but falls behind in detecting micro-calcifications [20]. The main problem associated with dedicated breast CT is scattered radiation, which jeopardizes an adequate quality image acquisition [14, 18]. The scattered radiation decreases the contrast and signal-to-noise ratio resulting in artifacts in the image [1, 21].

Furthermore, the image produced by conventional CT represents the x-ray attenuation map. The difference in the attenuation that describes different tissues is the source of the fundamental contrast in this imaging modality. The attenuation coefficient (μ) is a function of the x-ray beam energy, atomic number and electron density of the material. Hence, μ cannot completely characterize the material [22]. The electron density and effective atomic number provide additional information and may facilitate diagnosis [23]. A number of studies to investigate the application of electron density for breast diagnosis have shown the potential to improve characterization of the breast tissue by using the electron density [24, 25]. Since, an

2

accurate representation of the imaged object is the goal of any imaging modality, a fuller characterization of the object material would be an advantage.

While CT has advantages, concerns associated with the dose delivered to patients during the procedure have been raised [26]. There are a number of ways to limit the radiation dose delivered during a CT imaging procedure. These include decreasing the number of projections, acquisition time and tube voltage. The implementation of these options creates an under-sampled dataset which leads to an image of suboptimal quality. Access to additional information might hypothetically offset the data under-sampling caused by the dose reduction techniques.

The production of scattered radiation during an x-ray imaging procedure is unavoidable. When traversing an object, primary x-rays interact with the material and produce scattered radiation. For cone-beam breast CT, a scatter-to-primary ratio has been reported to be as high as 1.5 [27]. Conventional x-ray imaging systems employ a variety of methods to remove the impact of this radiation (anti-scatter grids, scatter compensation methods etc.) [28, 29]. However, as the scattered radiation is always present, considering scatter as an additional source of information and using this otherwise contaminating signal is of interest [30]. The information obtained from the scattering signal would aid in fully characterizing the imaged material and could potentially facilitate a decrease in the dose delivered during x-ray imaging procedure.

The electron density composition of the object can in principle be extracted from the Compton scattering signal since the intensity of a single Compton scattered signal is proportional to the electron density of the scattering medium. The core concept of Compton scatter tomography (CST) is the recovery of the electron density map of the object constituents using Compton effect.

The main contribution of the current work is the investigation of the feasibility of Compton Scatter imaging in a fan-beam 2D breast CT geometry. This work provides:

1. The introduction of multi-projection Compton scatter tomography (MPCST)

2. The assessment of the reconstructed electron density image quality

3. The investigation of the system specifications that affect the quality of the reconstructed image and

4. Identification of the methods to improve the quality of this image and the tradeoffs associated with it.

The design of the system investigated in this work is modeled after a 2D cross-sectional view of a breast CT geometry. Energy sensitive, photon counting detectors are arranged on the periphery of the primary fan-beam to detect scattered photons. The electron density distribution in the imaged object is obtained using spectral information of the Compton scattering signal that is recorded at a defined location. The assessment of the effect of the detector energy resolution, detector size and the number of projections on the image quality, specifically on the contrast and spatial resolution of the reconstructed electron density image, is performed for a specified geometry using a number of idealized conditions and simplifications. Though not immediately applicable to clinical practice, the results of this work will enable further investigation of the impact of departing from these assumptions, including the use of a mono-energetic source and lack of attenuation and multiple scatter, to be addressed while using an optimal detector specifications and projection number.

A brief overview of the subsequent chapters of this thesis:

Chapter 2 consists of the theoretical background relevant to the research topic.

Chapters 3 and 4 represent the core of the contributions of this thesis. Chapter 3 is based on a manuscript published in the Journal of X-Ray Science and Technology, Vol. 22(1), T. Chighvinadze and S. Pistorius, *The Effect of Detector Size and Energy Resolution on Image Quality in Multi-Projection Compton Scatter Tomography*, p.113-128. (Copyright 2014 with permission from IOS press). It introduces multi-projection Compton scatter tomography (MPCST) based on the algorithm previously developed for a single-sided industrial application. MPCST improves the reconstructed image quality by combining images obtained at different projection angles. This work investigates the tradeoffs between the size and energy resolution of the photon counting energy sensitive detectors for a fixed number of projections.

Chapter 4 describes the impact of the projection number on image quality in Compton scatter tomography (CST). In this imaging modality, even a single projection can produce an adequate quality image under idealistic assumptions, which include detectors with high energy and spatial resolutions. The ability to produce an image from a single projection differs conceptually from CT where a number of projections are needed to obtain an image. Hence, the conventional requirement for the number of projections defined for CT is not applicable to CST. In CST, the finite spatial and energy resolution of realistic detectors has an effect on the reconstructed image quality. Non-ideal specifications of the detector result in incomplete information due to the under-sampled data which in turn leads to suboptimal image quality. Therefore, this work investigates the effect of the number of projections on the reconstructed image quality to minimize the effects of the non-ideal features of the system.

Chapter 5 summarizes the findings of our work and suggests areas for future research.

CHAPTER 2. Theoretical Background

2.1. Interaction of x-rays with matter

The photons that traverse a medium without interacting are referred to as transmitted photons and represent primary radiation (Figure 2.1(a)). The x-ray photons that do interact with the material while traversing it undergo scattering or get absorbed. At the energy range characteristic of diagnostic x-ray imaging $(20 - 140\,\text{keV})$ there are three interaction processes that can take place: photoelectric absorption, Rayleigh (coherent) scattering and Compton (incoherent) scattering (Figure 2.1).
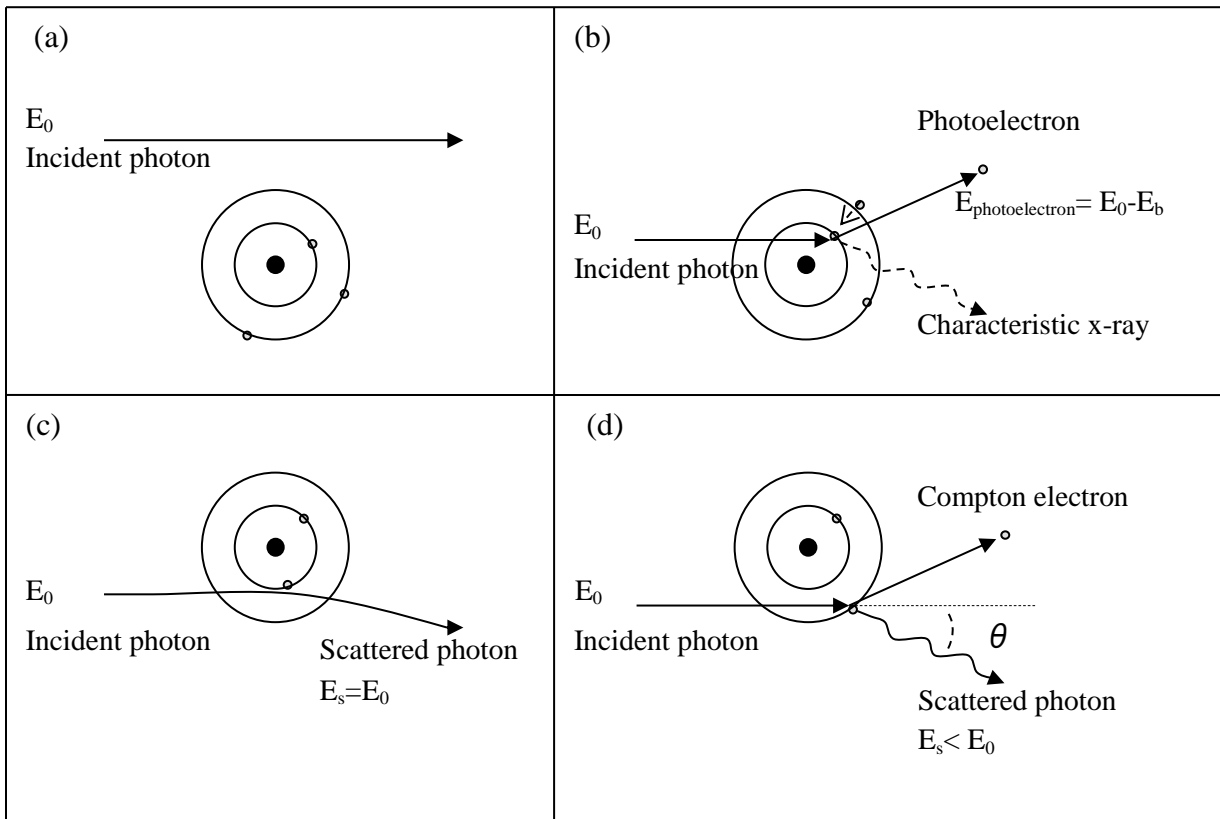
Figure 2.1. Illustration of the processes that take place when the x-ray photons propagate through the medium at the diagnostic energy range. (a) A photon passes through material without interacting. There is no attenuation. (b) Photoelectric absorption. (c) Rayleigh scattering. (d) Compton scattering.

During photoelectric absorption, the incident photon is absorbed while interacting with the electron of an atom. Because of this interaction, complete energy of the photon is transferred to the electron, which is ejected from the atom. The energy of this ejected photoelectron equals the difference of the incident photon energy and the electron binding energy ($E_{photoelectron} = E_0$ - E_b). The shell vacancy created, as a result of this process, is filled with an electron from the outer shell. Consequently, a characteristic x-ray photon is produced, with the energy of this photon given by the difference of the binding energies of the electron that left the vacancy and the one that filled it (Figure 2.1(b)).

When the incident photon interacts with a whole atom, it can be scattered with only a slight change in the direction and essentially with no change in the energy. This type of interaction is referred to as Rayleigh scattering (Figure 2.1(c)).

Compton scattering is an interaction of the incident photon, the energy of which exceeds the electron binding energy, with an "unbound" electron. During this process, part of the x-ray energy goes to the electron, which subsequently is ejected. The remainder of the energy is carried away by the photon that gets scattered (Figure 2.1(d)). The Compton equation that relates the energy of the incident photon with the energy of the photon that has been scattered at an angle θ is given as follows:

$$E_S = \frac{E_0}{1 + \dfrac{E_0}{m_0 c^2} \cdot (1 - \cos\theta)} \qquad (2.1)$$

where E_S is the scattered photon energy, E_0 is the incident photon energy and $m_0 c^2$ is the rest mass energy of the electron (511 keV).

These interaction processes contribute to the attenuation of the incident x-ray beam and ultimately to the contrast of the image. Different tissues attenuate at different degree, which facilitates differentiation between them. Assuming a mono-energetic beam passing through a slab

of material with thickness l [cm], the linear attenuation coefficient (μ [cm^{-1}]) can be defined from the intensities of the incident and transmitted beams (N_0 and N_t respectively) using the following expression:

$$N_t = \exp\left\{-\int_L \mu(l)dl\right\} \cdot N_0 \qquad (2.2)$$

where L is the path length. This expression is referred to as *Lambert-Beers* equation.

Total x-ray beam attenuation takes into account the contribution from the photoelectric, Rayleigh and Compton effects. Thus, the value of the total attenuation is defined from the radiation that exits the object and represents the sum of the attenuations corresponding to each of the listed interaction processes:

$$\mu = \mu_{Photoelectric} + \mu_{Rayleigh} + \mu_{Compton} \qquad (2.3)$$

Depending on the incident photon energy and the atomic number of the material, i.e. the medium where the interaction takes place, the contribution from either the photoelectric interaction or from the Compton scattering will be dominant. Rayleigh scattering is relevant at low energies [31, 32]. For instance, for an incident beam of 55 keV energy and a material representing breast tissue (low Z) the dominant interaction process is Compton scattering (~ 86%).

2.2. Conventional x-ray imaging

In conventional x-ray imaging techniques, the detected signal represents x-rays that have passed through the object from the source to the detector. In radiography, registered radiation intensity is a cumulative effect of the attenuation of the structures within the imaged body along

the linear path of the x-rays, from the source to the detector. Consequently, the obtained image portrays superposition in the direction of the beam [33].

2.2.1. Introduction to Computed Tomography

X-ray Computed Tomography (CT) is a noninvasive imaging modality where a superposition of the intertwined structures within the imaged object is not a concern, which is contrary to the planar imaging modalities (e.g. mammography) [34]. In CT, the data acquisition is performed as the source and detectors revolve around the object and acquire measurements from each projection angle. The scanning geometry differs depending on the generation of the scanner yet the requirement of a full 360^0 revolution around the object is common for all (Figure 2.2). Figure 2.3 illustrates the schematics of the third generation CT scanner, the most frequently used generation. The x-ray fan-beam, which radiates from the source, covers the whole slice of the object while traversing it, subsequently being recorded by the detector on the opposite side of the object. The recorded signal, 1D profile of the intensity, portrays different degrees of attenuation undergone by the beam while traversing the object (Figure 2.3(b)). As a result, the physical parameter obtained from the reconstruction is a linear attenuation coefficient. The degree at which the beam is attenuated depends on the material and the distance crossed. In order to have an adequate representation of the attenuation distribution within the object, the attenuation profile is acquired from multiple directions. In this imaging modality, the number of projections and the number of views per projection affect spatial resolution of the reconstructed image. A set of acquired data results in a 2D reconstructed image of the object. This digital image depicts a slice through the object in the axial direction (Figure 2.4) and describes the attenuation distribution within a defined cross-sectional view of the object.
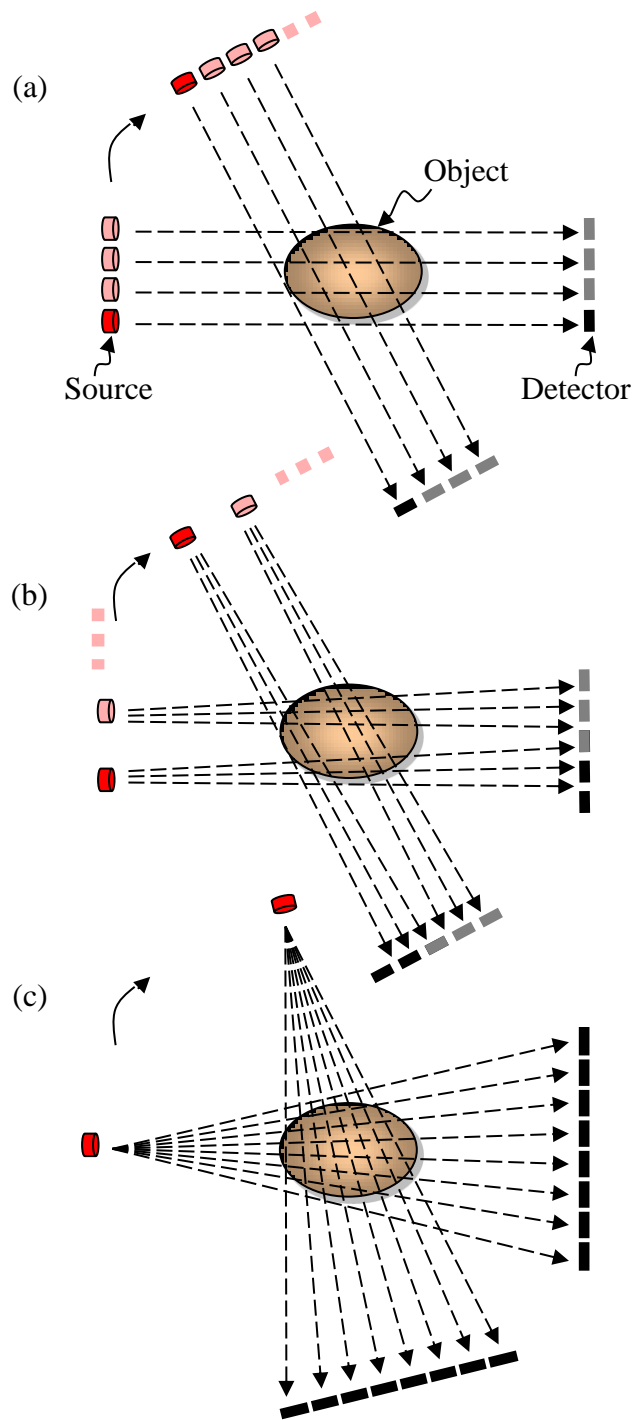
Figure 2.2. Schematics of the image acquisition in the first (a), second (b) and third (c) generation CT scanners. (a) A pencil-beam producing x-ray source and detector translate to cover the object and then rotate. The translation procedure is repeated for every projection angle. (b) A small angle fan-beam producing x-ray source and the corresponding detector array translate to

cover the object, and then rotate and repeat the procedure. (c) A fan-beam of x-rays covers the whole object slice and together with a detector array revolves around the object.
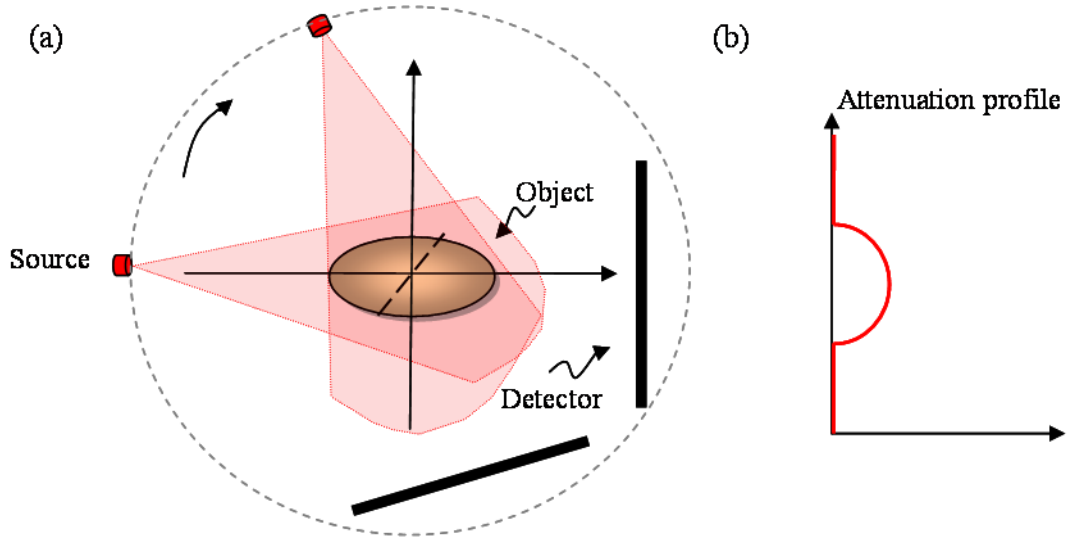
Figure 2.3. (a) Diagram of the data acquisition in a third generation CT, where a fan-beam producing x-ray source and an array of detectors that are placed on the opposite sides of the object, rotate around this object. (b) Attenuation profile of the beam after it passes through a homogeneous circular object. The profile is obtained for a single projection.
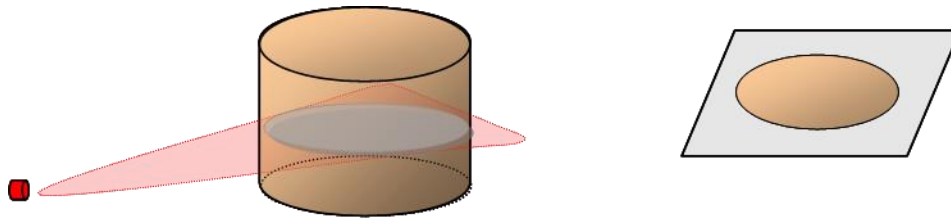
Figure 2.4. A hypothetical object to be imaged and a slice of this object that can be obtained by third generation fan-beam CT.

2.2.2. Mathematics of CT

The mathematical concept that gave rise to image recovery from x-ray projections was conceived by Austrian mathematician J. Radon in 1917. The cornerstone of this concept is that a function describing an object, e.g. distribution of the material or its properties within this object, can be represented as a set of its line integrals. Subsequently, computation of the Radon transform and its inverse leads to the recovery of the object and its constituents from the projection data. Hence, the basis of the tomographic image formation is the computation of the Radon transform and its inverse.

In CT, an image formation involves reconstruction from the projection data that is acquired after an x-ray beam propagates through the object (see Figure 2.3). A set of intensity profiles obtained at each projection represented as a function of the corresponding projection angle provides a raw data set. This data set is referred to as a Radon space of the object or a sinogram (Figure 2.5) [34]. Figure 2.6 illustrates the object to be imaged, acquisition of the beam attenuation profiles through this object and sinograms obtained using 4, 8, 15, 45, 90 and 360 projections.
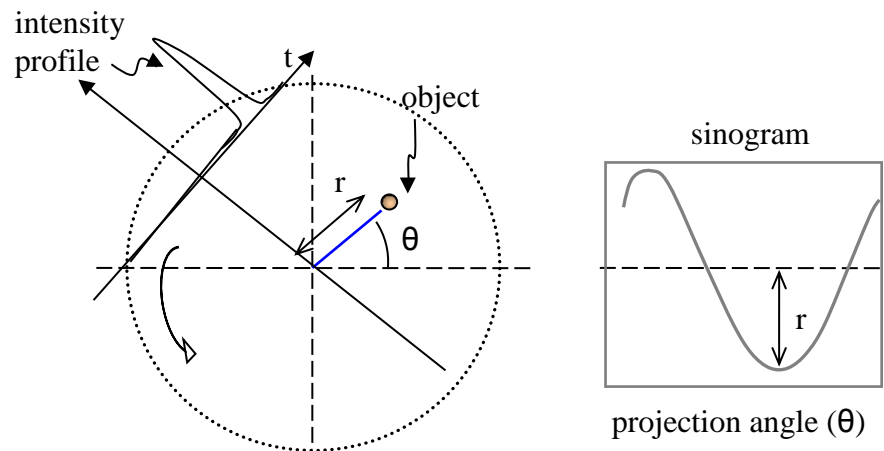
Figure 2.5. Schematics of a sinogram formation. (The image is modified from: [1]).

(a) Original Image

(b)

(c)

4 Projections   8 Projections   15 Projections

45 Projections   90 Projections   360 Projections
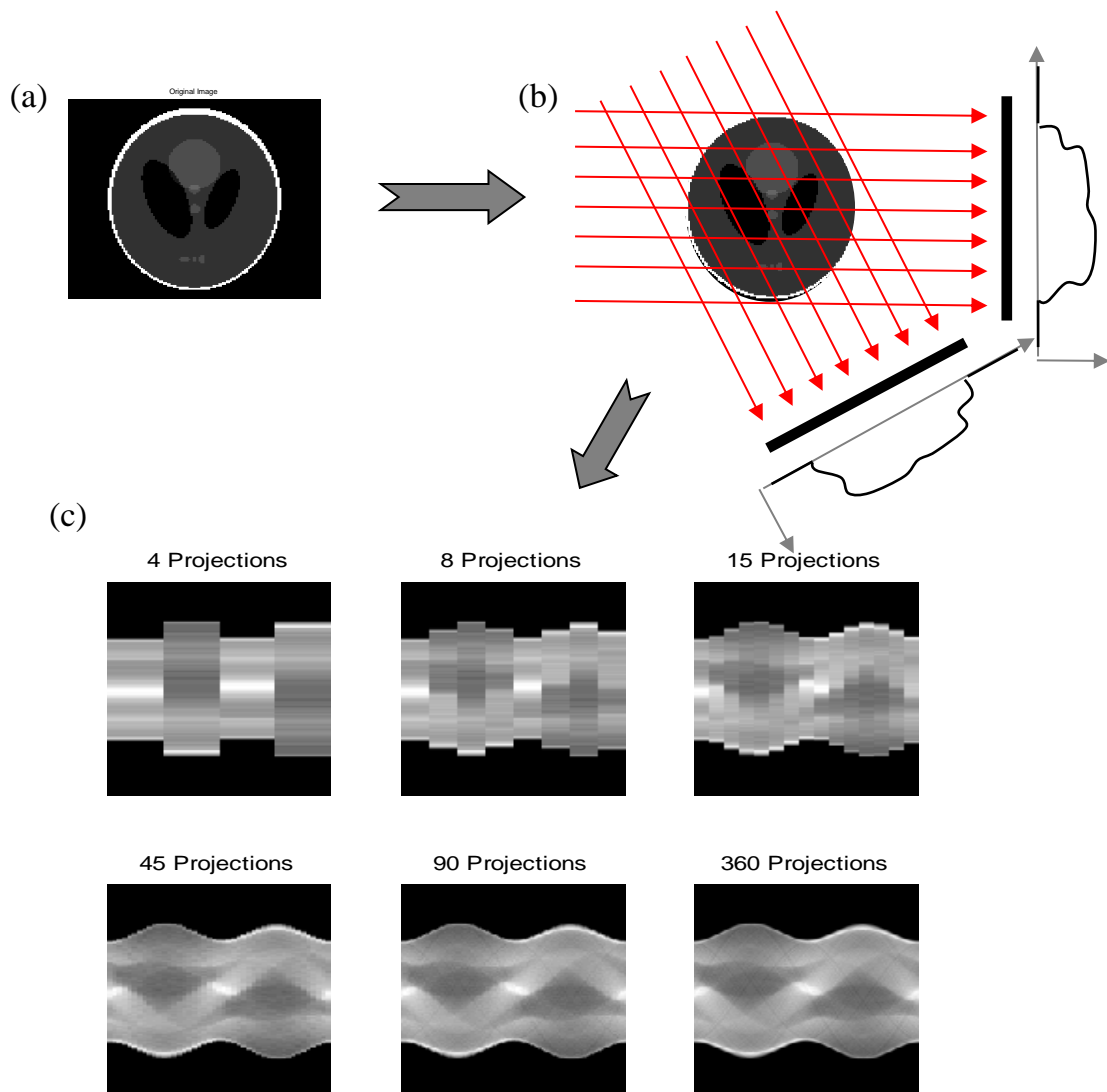
Figure 2.6. (a) Illustration of the object (Shepp-Logan phantom), (b) acquisition of the beam attenuation profiles and (c) sinograms (radon transforms) of the phantom obtained using 4, 8, 15, 45, 90 and 360 projections (from top left to the bottom right).

Hence, the projection data is represented as a line integral of the linear attenuation coefficient along the x-ray photon propagation direction. The attenuation of the object can be defined from the *Lambert-Beers* equation (Equation 2.2) by taking the logarithmic ratio of the transmitted and incident photons.

$$P_{projection} = -\ln\left(\frac{N_t}{N_0}\right) = \int_0^L \mu(l)\,dl \qquad (2.4)$$

Figure 2.7 illustrates the view of the transverse slice of the imaged object and the parallel-beam geometry CT. It describes the Fourier slice theory, depicting correlation between Fourier transforms (FT) of the projection and the object. This theory states that the Fourier transforms of the $P_\theta(t)$ projection of the object (described by $\mu(x,y)$) corresponds to a line in a 2D FT of this object [1, 2]. Given that the object is described by a linear attenuation coefficient $\mu(x,y)$ and the projection is represented by a set of line integrals, the Equation 2.4 can be rewritten as follows:

$$P_\theta(t) = \int_{-\infty}^{\infty} \int_{-\infty}^{\infty} \mu(x,y)\,\delta(x\cdot\cos\theta + y\cdot\sin\theta - t)\,dx\,dy \qquad (2.5)$$

where θ corresponds to the x-ray source and detector rotation angle and t to the distance from the center of rotation along the projection. $P_\theta(t)$ defines the projection data in terms of the Radon transform of the $\mu(x,y)$ function representing the object. In order to reconstruct the image a computation of the inverse Radon transform of the projection data is required.

(a)

(b)

Projection

y

Fourier transform

θ

μ (x,y)

L

x

u

θ

v

Object space

Fourier space
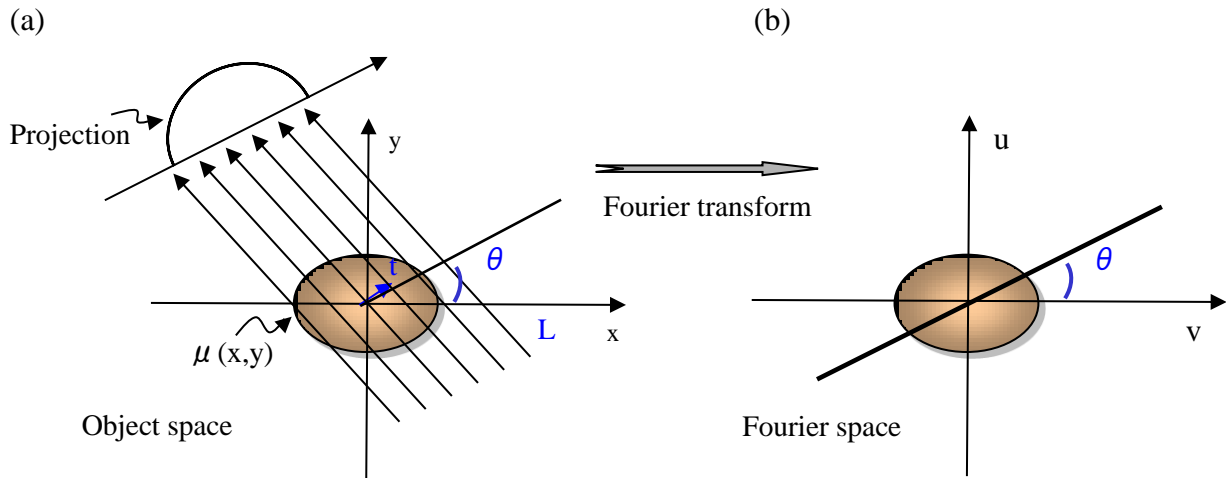
Figure 2.7. Illustration of the Fourier slice theory. It shows the relation between Fourier transforms (FT) of the projection and the object. The FT of the $P_\theta(t)$ projection of the $\mu(x,y)$ object corresponds to a line in a 2D FT of the $\mu(x,y)$ object [1, 2].

Reconstruction algorithms can be categorized as analytical and iterative. The analytical approach centers on the Fourier slice theory and employs a direct method for the reconstruction technique, using exact correlation between the input (projection data) and the output (reconstruction). The iterative reconstruction algorithms assume a model of gradual convergence through multiple repetitions of the process while introducing adjustments to the initial estimate.

The filtered backprojection (FBP) is an analytical reconstruction technique defined by an inverse Radon transform. It was introduced in late 1960's and remains (with modifications) extensively used in the advanced CT scanners [2, 35]. Using the measured data as the input information, the FBP algorithm solves the problem of mapping back the values of the linear attenuation coefficient within a cross section of an object. Conceptually, to reconstruct an image, the measured projection data ($P_\theta(t)$) is filtered, i.e. multiplied by an appropriate mathematical function that enhances high frequencies of the signal, and smeared back over the line connecting the source and detector. The purpose of the filter function is to sharpen the image that is

otherwise a blurry representation of the imaged object. Mathematically this process can be expressed as follows [2]:

$$\mu(x, y) = \int\limits_{0}^{\pi} \int\limits_{-\infty}^{\infty} FT\{P_\theta(t)\} |w| e^{i \cdot 2\pi t} dw d\theta . \qquad (2.6)$$

It is to be noted that, the path of the backprojection is not limited to a straight line and the object function to the linear attenuation coefficient. The path can be represented by a curve while the object can be described by the electron density values [36, 37]. Chapter 3 illustrates the images obtained using this notion.

2.2.3. Sampling requirement in CT

FBP-like algorithms are the most widely used algorithms for image reconstruction from projection data. In this technique, population of the data grid in the frequency domain is accomplished by obtaining multiple projections and performing their Fourier transform (see Figure 2.7). If the projection data is under-sampled it results in incomplete information in the Fourier space, which leads to the degradation in the image quality. For example, Figure 2.8 demonstrates the images reconstructed via FBP algorithm using 4, 8, 15, 45, 90 and 360 projections. The figure indicates that insufficient angular sampling results in less than adequate quality of the reconstructed image.

4 Projections	8 Projections	15 Projections

45 Projections	90 Projections	360 Projections
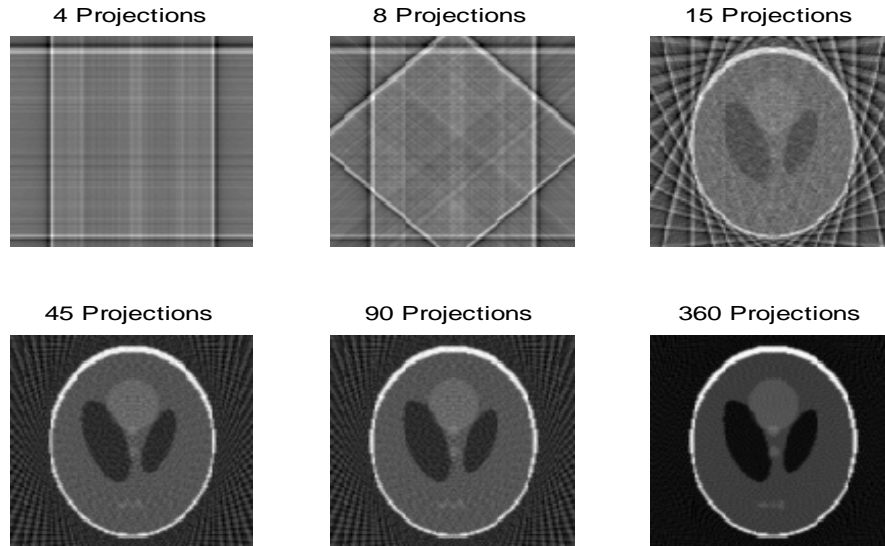
Figure 2.8. The images reconstructed using FBP algorithm using 4, 8, 15, 45, 90 and 360 projections (from top left to bottom right). The dimension of the image matrix is 128×128 mm^2.

The Shannon-Nyquist sampling theory states that in order to have an adequate representation of a signal, sampling should be twice that of the highest frequency component of the signal [1]. Aliasing distortions, caused by under-sampling may otherwise occur [2]. With that in mind, conventional third generation fan-beam CT performing a complete 360^0 rotation, has a sampling requirement for the minimum number of projections (N_{min}) which depends on the size of the region of interest and the spatial resolution to be achieved [38]:

$$N_{min} = \frac{2 \cdot \pi \cdot D \cdot u}{1 - \sin\left(\frac{\gamma}{2}\right)} \quad (2.7)$$

D – maximum diameter of the object to be imaged

u – maximum spatial frequency to be resolved

γ – angle of the fan-beam
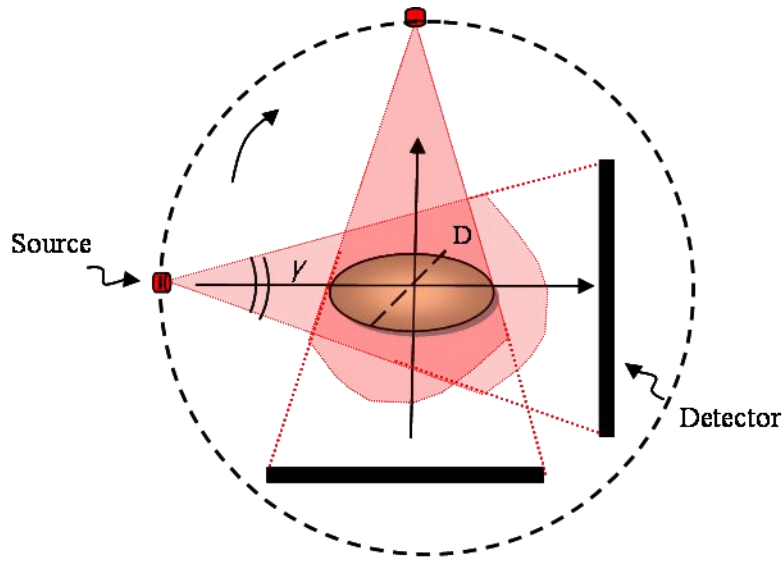
Figure 2.9. The set-up of the conventional third generation fan-beam CT where the source and detectors rotate around the isocenter of the system, and the object to be imaged is placed in the centre of the system.

For example, for a 10 cm diameter object with a 0.1 cm diameter insert that is to be resolved ($D = 10$ cm, $u = 1/0.1$ cm^{-1} and $\gamma = 31.8^{0}$), the required number of projections is about 865.

In practice, the number of projections are selected using other experimental factors in addition to the aliasing criteria [1, 2]. These factors include the finite source and detector sizes, as the latter results in band-limited projection data. These conditions relax the sampling requirement as they smooth the artifacts that result from under-sampling, allowing the use of fewer than the theoretical minimum number of projections (N_{min}) defined by Equation 2.7. The required number of projections is typically obtained from empirical measurements performed under practical conditions rather than from a strict application of Equation 2.7. The number of projections used in commercial CT is about 1000 per full 360^{0} rotation [1, 2].

2.2.4. Breast CT

CT is a constantly evolving modality introducing new technologies and expanding upon old ideas [39]. Breast CT is an integral part of the evolution of this powerful imaging tool. Significant advancement in breast CT imaging relates to improvements in detector technology [16, 17]. The work published by Boone *et al*. in 2001 [16] marks a milestone in the development of this imaging modality. The University of California, Davis Medical Center, was the first to start patient scanning in 2004 [20]. In March of 2014, 3D breast CT (the Konning Breast CT), which was developed at the University of Rochester Medical Centre, was approved as a medical imaging device by Health Canada [40, 41]. Furthermore, the review work done by Karellas *et al*. in 2008 investigates perspective applications for breast cancer imaging and suggests that an application using x-rays in the imaging will be the primary modality for screening in the next decade [42].

The image quality and the dose pertaining to breast CT was investigated by Boone *et al*. [16]. The design of the dedicated breast CT scanner presented in that work includes a cone-beam geometry and a flat-panel detector (Figure 2.10). The layout of the system is similar to the one used in the first fan-beam geometry scanner which was introduced for breast imaging in the 1970's [15, 43]. Dedicated breast CT allows 3D imaging of the breast with isotropic resolution yet suffers from high level of scatter radiation. This radiation has a deleterious effect on the image quality causing the cupping artifact and decreasing the contrast. Scatter radiation represents a major problem in this imaging modality.

Whenever imaging is performed using x-rays, the process is accompanied by production of scattered radiation, necessitating methods to address this fact. Therefore, the issue of scattered radiation is and will remain a relevant topic.
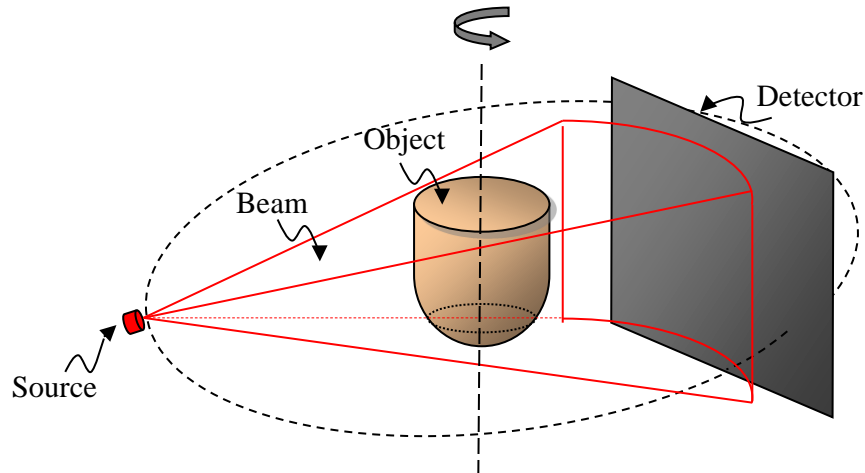
Figure 2.10. Schematics of the breast CT scanner. A cone-beam producing x-ray source and a flat-panel detector rotate around the pendant breast.

2.3. Imaging using scattered radiation

Current x-ray medical imaging employs primary radiation and relies on non-interacting photons, yet during this procedure the production of scattered radiation is inevitable. In the diagnostic energy range for the medium representing a tissue, over 50% of the interactions are typically scattering events [44]. The scattering process causes the incident photon to deviate from the direction of its propagation via one of the processes described in section 2.1. Scatter imaging utilizes the signal that is already present and considered to be a nuisance. A review work published by Theodorakou and Farquharson [45] describes the relevance of scattered radiation for soft tissue characterization. For CT applications, it has been demonstrated that Rayleigh and Compton scattering signals can be used for tissue analysis [46-48].

Depending on the type of physical interaction undergone by the x-ray photons traversing the medium (see section 2.1) one of the following will occur: x-ray fluorescence (photoelectric absorption), x-ray diffraction (Rayleigh scattering) or Compton x-ray scattering (Compton scattering). For an incident beam within 20 keV to 140 keV energy range and a low atomic

number material such as breast tissue ($Z_{ef.} \approx 7$), the dominant interaction process is Compton scattering.

2.3.1. Compton scatter imaging

Compton scatter imaging for medical application dates back to the work performed by Lale in 1959 [3]. When an object consists of structures that have similar density, the transmission imaging is impaired since it relies on the difference in the x-ray absorption by the material. Consequently, this leads to a small difference in the contrast between the structures in the reconstructed image. In this case, Compton scatter imaging would be advantageous as it is more sensitive to the density variation in the material compared to the primary imaging. Compton scatter imaging yields to the electron density distribution within an imaged object, while transmission imaging produces a map of the attenuation distribution.

Compton scatter imaging has been studied by various groups and was suggested as an alternative or a complementary application to conventional transmission imaging. The applications of Compton scatter imaging include medicine and industry; it can be used for historical exploration and agricultural studies [49-51].

The system suggested by Lale consists of a pencil-beam producing source of photons and a collimated detector for measuring scattered radiation (Figure 2.11(a)). This system provides electron density at a point along the incident beam. Following Lale's pioneering work on Compton scatter imaging for medical application, Farmer and Collins further explored this imaging modality and suggested the use of energy sensitive detectors (Figure 2.11(b)) [4]. Discrimination of the energy and scattering angle enables to define the electron density distribution along the path of the incident pencil beam.
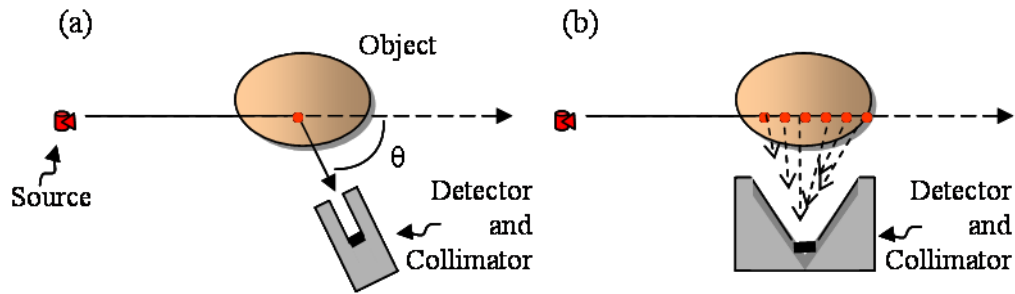
Figure 2.11. (a) Illustration of the system advocated by Lale [3]. It measures Compton scattering signal and provides electron density at a point defined by the incident pencil beam and an acceptance angle of the collimated detector. (b) Schematics of the system introduced by Farmer and Collins [4]. The system uses a wide-angle collimated energy sensitive detector and provides electron density along a line defined by the primary pencil beam.

Kondic introduced the idea of recovery of the scattering location over a circular arc using the Compton relationship [52, 53]. The mathematical basis for analytical restoration of a function from its integrals taken along curved paths was provided by Cormack [36, 37].

Work presented by Norton in 1994 marked a milestone in the development of CST. It builds on the mathematical apparatus devised by Cormack [36] and introduces a computationally convenient filtered backprojection approach for the reconstruction from single Compton scattering signal. In this analytical algorithm, the scatter signal is backprojected over an isogonic curve that connects the source and detector and is defined by the relevant scattering angle, which relates to the particular scattering energy (Figure 2.12) [54]. Norton's approach was developed for an industrial, single-sided application. The proposed scanner consists of a fixed γ-ray source and an energy sensitive point detector that moves along a line passing through the source [55].
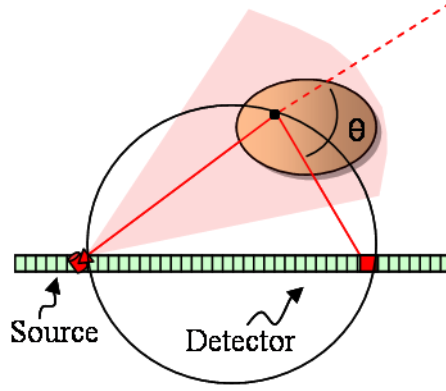
Figure 2.12. Illustration of the source, energy sensitive detector and isogonic curve defined by the particular energy of the measured scatter signal. This circular curve connects the source and detector, and it defines the path where the point of origin of the scattered photons is located.

The correlation between the number of incoherently scattered photons (N_s) and the number of incident photons (N_0), which also accounts for the density of the scattering points, the probability and the direction of its occurrence, can be determined by [56]:

$$N_s = N_0 \cdot \rho_e \cdot dv \cdot \frac{d\sigma}{d\Omega}(E,\theta) \cdot d\Omega \qquad (2.8)$$

where ρ_e is the electron density of the material, dv is the volume of the site where scattering takes place, $\frac{d\sigma}{d\Omega}(E,\theta)$ represents the Klein-Nishina differential cross-section and $d\Omega$ is the solid angle subtended by the detector. The Klein-Nishina cross-section is defined by:

$$\frac{d\sigma}{d\Omega}(E,\theta) = \frac{r_0^2}{2} \cdot \left(\frac{E_s}{E_0}\right)^2 \cdot \left(\frac{E_s}{E_0} + \frac{E_0}{E_s} - \sin^2\theta\right) \quad (2.9)$$

In this equation r_0 is the classical electron radius ($r_0 = 2.82 \times 10^{-13} [cm]$) [31]. E_0 represents the incident photon beam energy and E_S the scattered photon beam energy, which are related by the Compton equation (see Equation 2.1).

The probability of Compton scattering defines the electron density of the material ($\rho_e [electrons/cm^3]$), which in turn is defined by the physical density of this material ($\rho [g/cm^3]$) as follows:

$$\rho_e = \rho \cdot N_A \cdot \frac{Z}{A} \qquad (2.10)$$

where N_A is Avogadro's number ($6.022 \times 10^{23} [mol^{-1}]$), Z atomic number and A atomic weight. For most elements, $A \approx 2 \times Z$.

Hence, from the measurements of the scattered radiation, the inverse problem in Compton scatter imaging reconstructs the electron density distribution in the imaged object.

CHAPTER 3. The Effect of Detector Size and Energy Resolution on Image Quality in Multi-Projection Compton Scatter Tomography (MPCST)

This chapter contains material that has been reprinted and adapted from the *Journal of X-Ray Science and Technology*, Vol 22, T. Chighvinadze and S. Pistorius, *The Effect of Detector Size and Energy Resolution on Image Quality in Multi-Projection Compton Scatter Tomography*, p.113-128, Copyright (2014) with permission from IOS press.

3.1. Introduction

Scattered radiation, traditionally considered to be noise that degrades image quality, is always present in x-ray imaging [30]. In some modalities (i.e. cone beam CT) the scatter-to-primary ratio can be as high as 150 % [27]. Correction techniques that attempt to remove the scatter typically do so at the expense of increased dose [28]. This has prompted the development of Compton scatter tomography (CST) which offers a complimentary method to conventional, attenuation based image acquisition which uses transmitted radiation [3, 57]. Compton tomography was first introduced in 1959 for megavoltage imaging [3]. For low atomic number materials at medical diagnostic x-ray energies, the electron density of the scattering material is proportional to the intensity of the Compton scattering signal [32]. This is the essence of CST.

The clinical application of CST has been hampered by the low signal strength of Compton scattering as well as the presence of multiple scatter, photon attenuation and noise in the projection data [58]. A number of methods, which achieve reasonable image quality, have been developed to address these limitations. They are, however, not suitable for the imaging geometry and radiation dose required of a clinical x-ray CT system [49, 59].

The scattered photon fluence can be improved by increasing the source strength or acquisition time; however, this results in an increase in patient dose, lower throughput and motion artifacts [58]. Low photon counting statistics of the scattering signal can also be overcome by increasing the size of the detector, but this reduces the resolution of the reconstructed image. Energy discrimination and collimation of the source and the detector have been used to reduce the effects of multiple scatter [4, 59, 60]. Single scatter reconstruction algorithms can be corrected for multiple scatter events using a factor which increases with object thickness or radiological path length [61]. For thicknesses less than one-mean-free path length, the need for the correction can be avoided altogether [62]. Attenuation reduces the intensity of the single Compton scattering signal and increases the noise in the data. Typical techniques for attenuation corrections include estimation of the attenuation directly using independent CT data, iterative methods, and "dual energy" methods [60, 63, 64]. However, an accurate account of pre- and post-scattering attenuation that modulates the signal still remains an open issue [58, 65].

The present work assumes only single Compton scattering of the photons and ignores the effects of multiple scattering and attenuation. Though both of these factors modify the single scattering signal, they can be accounted for without significantly affecting the results of this work. While the presence of multiple scatter increases the signal, attenuation decreases it and the optimal detector characteristics are not strongly affected by small changes in the incident fluence [66]. Alpuche Aviles et al. [67] showed that it is possible to reconstruct an object from multiple scattering using a single scatter model. While qualitatively correct, the image overestimated the electron densities. Subsequent work by the same group [61] achieved correct reconstructed values by using an empirical correction to the single scattering model. An improvement in the reconstructed image contrast was obtained. A similar approach will be taken with this work.

Compton tomography is a multi-dimensional problem and while ongoing research has improved the image quality of CST, these studies have not explored the influence of the number of projections, imaging geometry, detector parameters, or the dose associated with these methods.

Our work aims to evaluate the feasibility of using multi-projection spectroscopic CST, by applying it to the geometry of x-ray breast CT. The current chapter presents the study of the influence of the detector size and energy resolution under the dose constraints appropriate for diagnostic breast imaging. Investigation of these specific aspects of the problem will allow further examination of the effects of multiple scatter, attenuation and the polyenergetic nature of the incident beam. Thus, this work provides a scientific evaluation of detector parameters while acknowledging the need to address the above issues before this approach can be considered clinically feasible.

The mathematical foundation required to analytically restore a function from its integrals taken along circular paths was initially presented by Cormack [36, 37]. The function of interest in Cormack's work was the attenuation coefficient, while in this work we are interested in the electron density of the object. Kondic suggested the use of the Compton relationship to trace the location of the scattering over a circular arc [52, 53]. For a given point source and detector position, and for particular scattered photon energy (E_s), the photon will have scattered from a point on the isogonic curve that connects the source and detector and is defined by the relevant scattering angle. Norton applied a computationally more convenient filtered backprojection approach [54] while Nguyen, Truong et al. further refined the concept of imaging using a scattering signal by carrying out Radon transforms on a set of circular arcs [68-71].

The reconstruction technique used in this work expands on Norton's [54, 55] concept by introducing a multi-projection approach which can be implemented for a clinical breast CT geometry. The spatial and energy resolution of the detector plays a pivotal role in the quality of the reconstructed image. When using detectors with an ideal energy and spatial resolution a good quality image can be reconstructed from a single projection. When the detector has a more realistic energy and spatial resolution (e.g. 1000 eV and 2×2 mm^2) the image quality varies across the image, due to under-sampling of the data caused by the finite resolutions of the detector (see

section 3.4.). By combining images obtained from different projection angles, the reconstructed image quality can be improved [72].

Our work uses an analytical model to simulate the system, radiation transport and dose to reconstruct transverse slices of a phantom for a dedicated breast CT geometry [66, 72]. This work demonstrates how the pixel size and the energy resolution of the detectors affect the quality of the reconstructed electron density image in multi-projection Compton scatter tomography, when the reconstruction is performed using backprojection over isogonic curves.

3.2. Background

The Compton equation relates the incident photon beam energy (E_0) to the energy of the scattered photons (E_S) and the angle of scattering ($\theta' = \pi - \alpha$). This relationship, which is described by Equation 3.1, forms the cornerstone of Compton tomography and is illustrated in Figure 3.1.

$$E_{SC} = \frac{E_0}{1 + \dfrac{E_0}{m_0 c^2} \cdot (1 + \cos \alpha)} \quad (3.1)$$

$m_0 c^2$ – the rest energy of the electron (511 keV).

The number of single Compton scattered photons, reaching a detector positioned at angle θ' with respect to the direction of the incident beam, can be expressed as follows [56, 73]:

$$N_s = N_0 \cdot \rho_e \cdot dv \cdot \frac{d\sigma}{d\Omega}(\theta') \cdot d\Omega \quad (3.2)$$

In Equation 3.2 N_0 is the number of incident photons, ρ_e and dv denote the electron density and

the volume of the scattering site, and $d\sigma\big/d\Omega(\theta')$ is the Klein-Nishina cross-section, that is the

scattering probability into $d\Omega$ solid angle subtended by the detector at θ'.
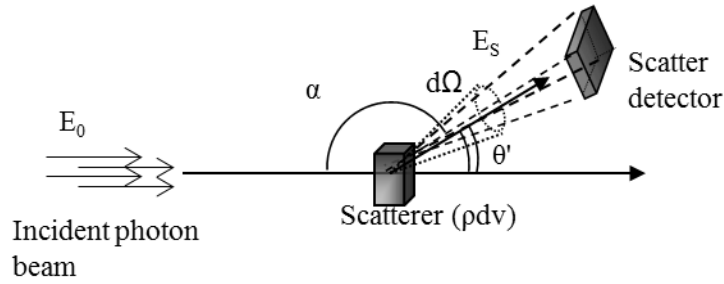
Figure 3.1. Principle of Compton scattering. Photon beam of energy E_0 after interacting with the scatterer is deflected through an angle θ' and continues to the detector with reduced energy E_S defined by Equation 3.1.

3.2.1. Image reconstruction from Compton scattering signal

When the positions of the point source and the point detector are known, and the scattering energy is defined, the scattering origin can be confined to the isogonic curve with the inscribed angle α, defined by the scattering angle [52-54].

Compton tomography as devised by Norton for single-sided application uses a filtered backprojection technique to recover the scattering signal over circles having the source as a common point. This is illustrated schematically in Figure 3.2.
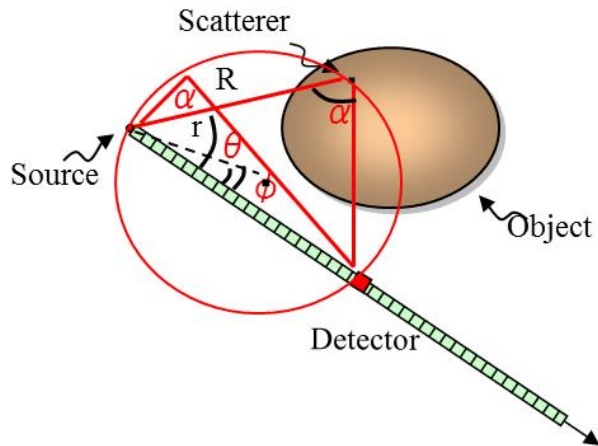
Figure 3.2. The photon is detected after being scattered at angle θ' (i.e. $\pi - \alpha$) due to Compton scattering. The track for backprojection (circle going through the source, scatterer and detector) is defined by the detected scattered photon energy and the locations of the source and detector.

There is a fundamental difference between data acquisition requirement for image reconstruction in traditional computed tomography and Compton scatter tomography. In CT to obtain a full data set a 360^0 revolution is needed, whereas in CST the data can be obtained from a single projection. Figure 3.3 illustrates schematics of the formation of a sinogram for third generation CT (Figure 3.3(a)) and a c-sinogram for CST (Figure 3.3(b)).
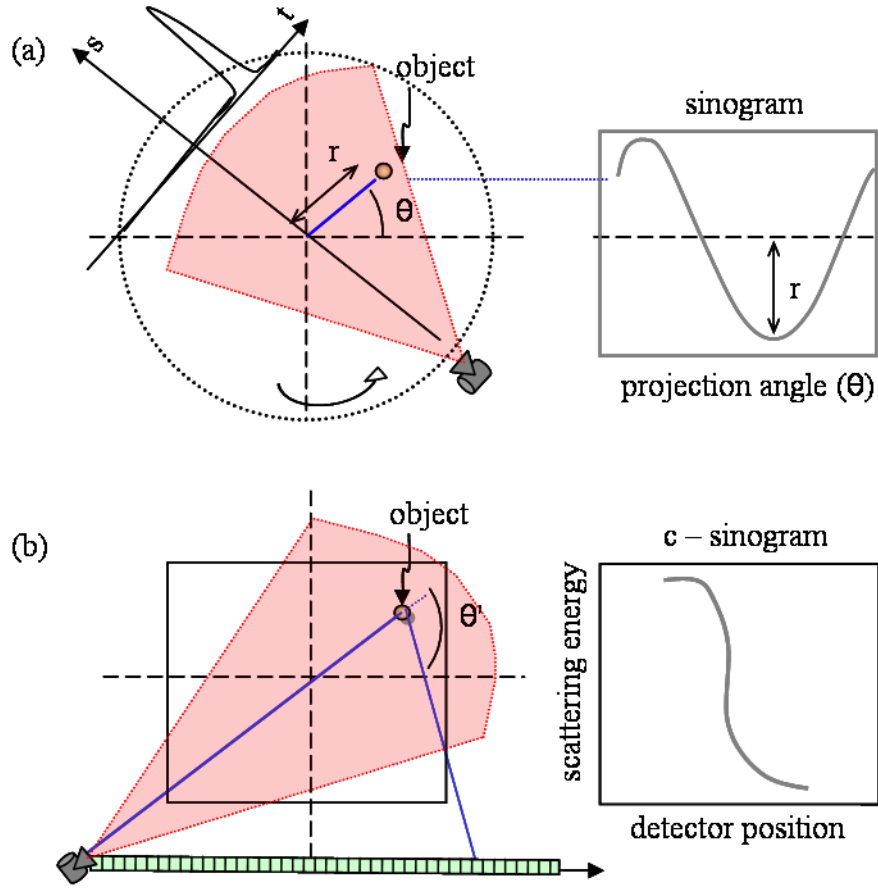
Figure 3.3. (a) Schematics of a sinogram formation for conventional, third generation CT. (b) Schematics of a c-sinogram formation for Compton scatter tomography. Note that in (b) scattering angle θ' directly relates to the scattering energy via Compton equation (Equation 3.1).

An inversion expression, for the recovery of the electron density of the imaged object, given by Norton [54] is as follows:

$$\rho_e = \frac{1}{\pi^2} \int_0^{2\pi} d\varphi \int_0^\infty r dr \left[\frac{N_s}{W(R,\theta;r,\varphi)} \right] . h[f] \qquad (3.3)$$

where $W(R, \theta; r, \varphi)$ is so called weighting function [56].

$$h[f] \equiv \int_{-\infty}^{\infty} e^{-iuf} |u| du \qquad (3.4)$$

$h[f]$ is the convolution kernel, where $f = R - 2r \cdot \cos(\theta - \varphi)$.

Here, backprojection is performed along $R = 2r \cdot \cos(\theta - \varphi)$ circular arcs, defined by the photon scattering energy and which pass through the source and detector, whereas in transmission CT, backprojection is along straight lines connecting the source and detectors.

3.2.2. Single vs. multiple projections

Under ideal conditions (point source and detector, ideal energy resolution, no noise etc.) the image can be reconstructed with a single projection using the algorithm described in section 3.2.1. For realistic energy and spatial resolutions, there is a noticeable variation in quality across the reconstructed image due to the inconsistent sampling of the data. Each of the characteristic features of the realistic system contributes to the degradation of the image quality. As a result, when reconstructing from a single projection using realistic values of the characteristic parameters of the system, the data space is sparsely populated. This can be compared to limited angle CT where the quality of the reconstruction is compromised due to under-sampling of the data space [74]. Using multiple projections essentially fills-in the missing data space, improving the ability to reconstruct an object.

3.2.3. Noise

In x-ray medical imaging, system noise introduces random variations in the image intensity and degrades the image quality. In particular, it obscures the visibility of small low contrast objects. For these modalities, quantum fluctuations in the x-ray beam are the dominant source of noise, and the photon counting statistics are described by a Poisson distribution [75].

In multi-projection Compton scatter tomography (MPCST), the noise variance is similar to that of conventional CT and is inversely proportional to the square root of the exposure received by the detector [76]. Increasing the number of incident photons can increase the signal-to-noise ratio (SNR) but is constrained by the biological effects due to the increased dose.

3.2.4. Detector

This application requires detectors with photon counting and energy resolving capabilities, operating at the diagnostic x-ray energy range of 20-140 keV. Solid-state detectors such as cadmium telluride (CdTe) and cadmium zinc telluride (CdZnTe) meet these criteria and can operate at non-cryogenic temperatures. The pixel size of CdZnTe detectors currently used in spectral CT is 1×1 mm^2 [77]. The energy resolution of CdZnTe detectors is several keV at 60 keV [78]. The gap between the theoretical limit and the current energy resolution of these detectors is being narrowed with developments in the technology. For example, the Caliste HD hybrid, a CdTe micro-camera developed for applications in astronomy has a full-width at half-maximum (FWHM) of 0.842 keV at 60 keV (at -10^0C) corresponding to an energy resolution of 1.4 % [79].

Within the limits imposed by the noise and the dose, the reconstructed image quality can be improved by reducing the size of the detector pixel and by increasing its energy resolution. By decreasing the size of the detector pixel, the visualization of small objects can be improved at the cost of an increase in noise, which reduces visibility of low contrast objects. The energy resolution of the detector also contributes to the blurring with larger energy bins resulting in increased blurring but lower noise, since more scattered photons will be registered.

This work investigates the optimal values for the given detector parameters aiming to achieve a suitable balance between noise and blurring that affects the quality of the image reconstructed from multiple-projection scatter data.

3.2.5. Image quality assessment

Image quality assessment provides information about the efficacy of the imaging technique. When the quality is low, the object of interest within the imaged body might be misinterpreted. An image is considered to be of a good quality if it closely resembles the imaged object.

While evaluating the reconstructed image quality, the main factors of interest are spatial resolution, contrast and noise. The common tools to describe these image characteristics include the modulation transfer function (MTF), peak signal-to-noise ratio (PSNR) and contrast-to-noise ratio (CNR) [75, 80, 81].

MTF can be calculated by taking the Fourier transform of the line spread function (LSF) and normalizing the outcome.

$$MTF = |FT(LSF)| \qquad (3.5)$$

$$PSNR = 20 \ \log_{10} \frac{\max(S_{i,j})}{\sqrt{MSE}} \qquad (3.6)$$

where $MSE(S,R) = \dfrac{1}{NM} \displaystyle\sum_{i=1}^{N} \sum_{j=1}^{M} \left(S_{i,j} - R_{i,j}\right)^2$

MSE – mean square error

S – original image intensity

R – reconstructed image intensity

$N \times M$ – size of the image

i and j – elements of the rows and columns of the image matrix

$$CNR = \frac{\frac{1}{A}\sum_{a=1}^{A}\rho_e{}^a - \frac{1}{B}\sum_{b=1}^{B}\rho_e{}^b}{\sigma} \qquad (3.7)$$

$\dfrac{1}{A}\sum_{a=1}^{A}\rho_e{}^a$ – mean electron density of the region of interest

$\dfrac{1}{B}\sum_{b=1}^{B}\rho_e{}^b$ – mean electron density of the background

σ – standard deviation of the background

3.3. Methods and materials

3.3.1. System design

The system geometry followed a breast CT design where a point source of x-rays was collimated to form a fan-beam, which traverses the imaging volume before interacting with the primary detector (Figure 3.4). The object to be imaged was placed at the isocenter of the system with a source-to-isocenter distance of 45 cm. The angle of the x-ray fan beam was 31.8^0.

A 55 keV mono-energetic photon beam was used in the simulation. At this energy, the dose per unit incident fluence is minimized [82]. The energy sensitive photon counting detectors were placed outside the periphery of the primary beam, in the same plane as the source. The length of the linear array of 2D detectors was 93.6 cm.
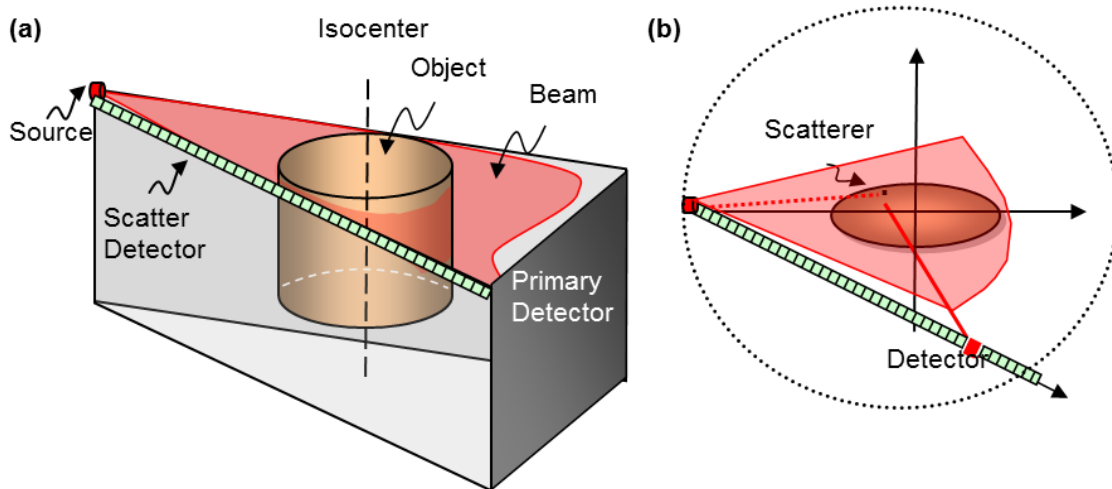
Figure 3.4. (a) Design of the system. (b) Transverse slice of the system, view from the top.

3.3.1.1. Phantom

In this study, a high contrast modified Shepp-Logan phantom illustrated in Figure 3.5 was used. It consists of ten superimposed ellipses [83]. The major and minor axes of the phantom were 11.6 cm and 8.8 cm respectively. The relative values of the inserts and the edge of the phantom, together with the percent difference between their values and the background, are given in Table 3.1. The Shepp-Logan phantom was originally created to emulate the human head. Here the constituents of this phantom were reassigned, to imitate the values of the electron densities of some artificial materials, including values that are comparable to those found in breast tissue.
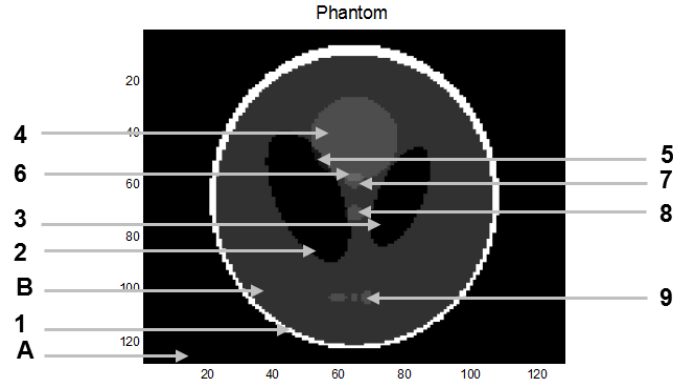
Figure 3.5. Modified Shepp-Logan phantom.

Table 3.1. Values of the components of the modified Shepp-Logan phantom

ROI	Relative value $\times 10^{23}$	Percent change relative to the background
A	0	- 100 %
B	2	background
1	10	400 %
2 & 3	0	- 100 %
4, 7, 8 & 9	3	50 %
5	1	- 50 %
6	4	100 %

* ROI – region of interest

The dose was limited to 12.8 mGy, which is the representative of the mean glandular dose for breast CT [84]. As discussed in the introduction of this chapter, this work considered only single Compton scattered photons, ignored multiple scattered photons and neglected attenuation. While these assumptions will limit the quantitative accuracy of the measurement of electron density the image quality is insensitive to these variations.

3.3.2. Data acquisition environment

The quality of the reconstructed image is affected by the detector energy resolution, detector pixel size, fluence/dose, size of the object to be imaged and the number of projection angles. In this work, the detector energy resolution and size were varied while holding the other parameters constant. Detector energy resolutions of 100 eV, 500 eV and 1000 eV and detector pixel sizes from 1×1 mm^2 to 3.5×3.5 mm^2 in 0.5×0.5 mm^2 increments were considered. Analytical simulations were performed to find the optimal values for these parameters.

The number of incident photons used in the simulation was determined from the imposed dose limit for the given energy and phantom size. For the purpose of this calculation, the considered object was assumed to have uniform content. The total dose due to 36 fan-beam projections of 55 keV photons incident on an object composed of breast tissue equivalent material with a diameter of about 10 cm was approximated as follows [75]:

$$D(E) = \Phi(E) \cdot E \cdot \left(\frac{\mu_{en}}{\rho}\right)_E \quad (3.8)$$

where $\Phi(E)$ is the fluence, E is the energy of the monochromatic x-ray photons and $\left(\mu_{en}/\rho\right)_E$ represents the mass energy absorption coefficient. The mass energy absorption coefficient for breast tissue, at an energy of 55 keV, was calculated from the work of Hubbell and Seltzer [85] and results in $\left(\mu_{en}/\rho\right)_{\text{Breast Tissue at 55 keV}} = 0.0208$ m^2/kg.

Although not explicitly modeled in our simulation, the detection area for scattering could be increased by measuring over a 2π geometry (Figure 3.6). In addition, the simulated object has a length (e.g. $1.5\times$r cm where r is the radius of the object); and the scattered photons would be collected from multiple slices. These factors would result in an increase in the signal due to the scattered photons.
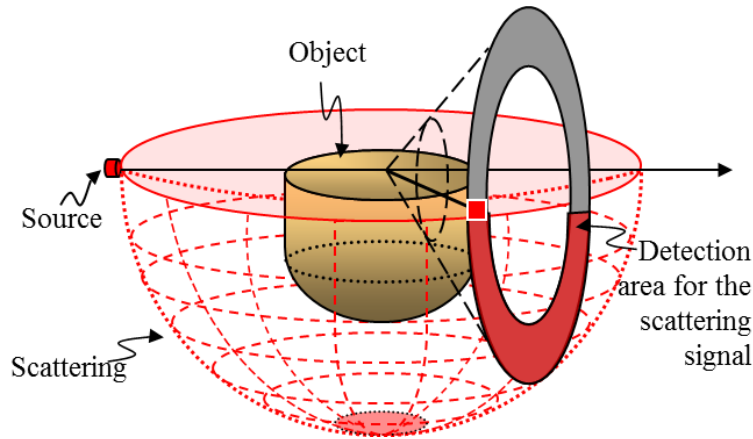
Figure 3.6. Detection of the scattering signal in the ultimate system.

Noise in the projection data follows Poisson statistics [75, 86]. Thus, the synthetic data generated by the analytical model was randomized with Poisson noise. The photon count value collected at the detector was assumed to be the mean, and a Poisson distribution was sampled for each detector element. To minimize the detrimental effect of noise on the image quality, the spatial and energy resolutions of the detector were optimized under limited dose conditions.

3.3.3. Reconstructed image acquisition

Image reconstruction from single projection data was described in section 3.2.1. In order to improve the overall image quality for realistic detector configurations a limited view image was reconstructed for each projection, and these were then averaged over all projection angles to obtain final image. In this study, 36 images were obtained from equiangular projections with 10 degree increments acquired over a 360-degree rotation. The size of each reconstructed image is 128×128 pixels with a resolution of 1 mm. The reconstructions were performed using MATLAB (The MathWorks, Inc., Natick, MA).

3.3.4. Evaluation of the reconstructed image quality

To measure the quality of the image reconstruction, the similarity between the original and reconstructed images was determined using the metrics given in section 3.2.5. The assessment was performed for the defined range of the detector pixel sizes and energy resolutions.

To obtain the MTF, the response of the system to a point input was acquired for each investigated system configuration. The profile of a point spread function (PSF) along one direction of the image matrix (row or column) was taken. The profile results in a line spread function (LSF), the Fourier transform of which leads to the MTF (Equation 3.5).

To estimate the visibility of the phantom inserts against the object/background in which they are embedded, the CNR was calculated for four structures within the phantom which are chosen as the regions of interest (ROI). To characterize the behavior of the visual quality metric due to different combinations of the detector parameters, the PSNR was calculated for each combination.

3.4. Results

Figure 3.7 provides visual perception of the projection data in conventional CT and single and multi-projection CST.
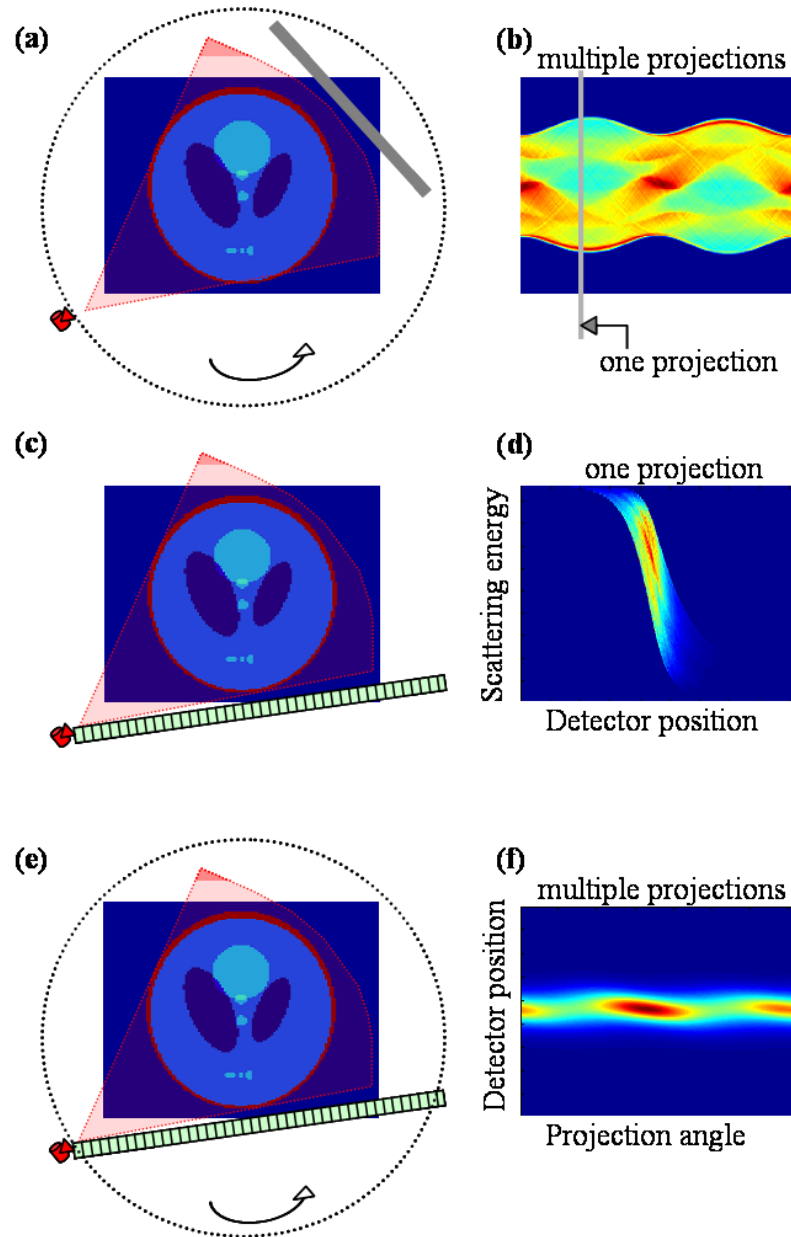
Figure 3.7. (a) Conventional, third generation, fan-beam CT and (b) sinogram obtained from data acquisition over 360 degrees. (c) CST and (d) c-sinogram obtained from data acquisition at a single projection. (e) MPCST and (f) c-sinogram obtained from data acquisition over 360 degrees.

Figure 3.8(a) shows the results of a reconstruction performed using a single projection in a noise free environment for high detector energy resolution (1 eV) and detector pixel sizes of 1×1 mm^2. Figure 3.8(b) illustrates an image reconstructed from a single projection when the energy resolution is 1000 eV. Figure 3.8(c) illustrates the results of using 36 projections to offset the under-sampling of the data due to finite detector resolution.

Figure 3.9 shows images reconstructed with a 1000 eV energy resolution for detector pixel sizes from 1×1 mm^2 to 3.5×3.5 mm^2 in 0.5×0.5 mm^2 increments, when the dose is not of concern. The results illustrate that the image quality improves as the spatial resolution of the detector increases.
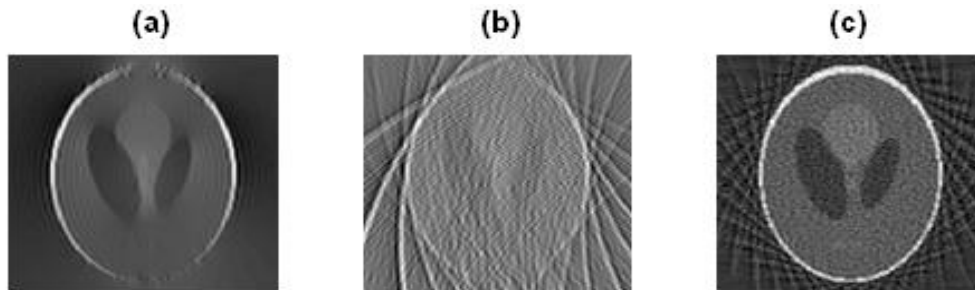
Figure 3.8. Reconstructed images of the modified Shepp-Logan phantom. The detector pixel is 1×1 mm^2. The detector energy resolution and number of projection used: (a) 1 eV and single projection; (b) 1000 eV and single projection; (c) 1000 eV and 36 projections.
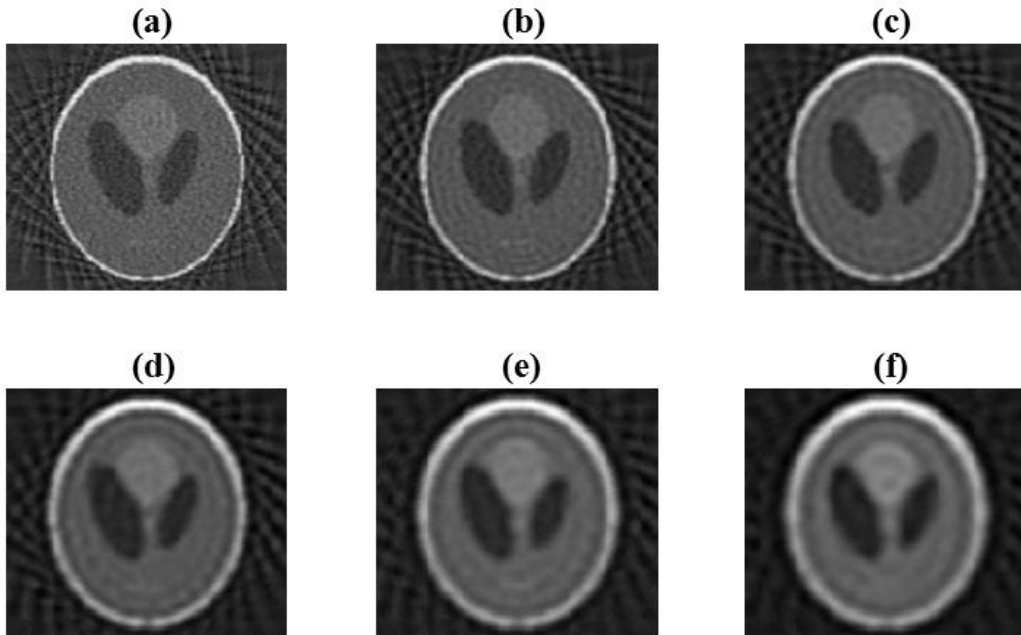
Figure 3.9. Reconstructed images of the modified Shepp-Logan phantom. From top left to bottom right, the size of the detector pixel increases from 1×1 mm^2 to 3.5×3.5 mm^2 with increments of 0.5×0.5 mm^2. The detector energy resolution for this set of the reconstructions is 1000 eV. This case has no dose constraint.

Figure 3.10 illustrates reconstructions obtained under similar conditions to Figure 3.9 but with the addition of noise, which is equivalent to that associated with a dose of 12.8 mGy. The optimal image is no longer obtained with the smallest detector and with the highest energy resolution. This is further confirmed in Figure 3.13.

Figure 3.11 shows reconstructions obtained under limited dose condition using detector with a 2×2 mm^2 pixel size and energy resolutions of 1000 eV, 500 eV and 100 eV.
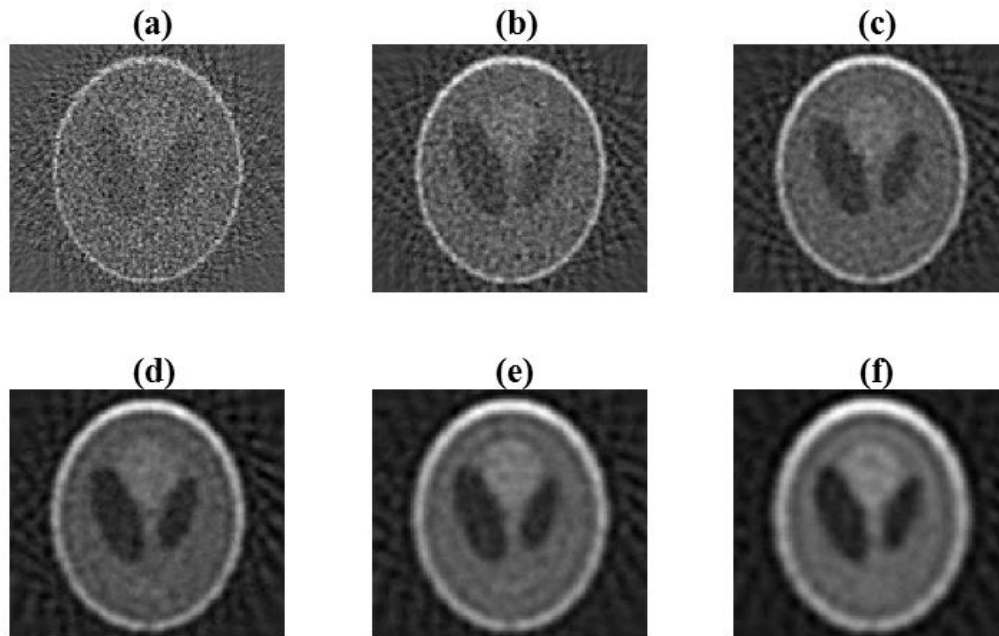
Figure 3.10. Reconstructed images of the modified Shepp-Logan phantom. From top left to bottom right, the size of the detector pixel increases from 1×1 mm^2 to 3.5×3.5 mm^2 with increments of 0.5×0.5 mm^2. The detector energy resolution for this set of the reconstructions is 1000 eV. The dose limit is 12.8 mGy.
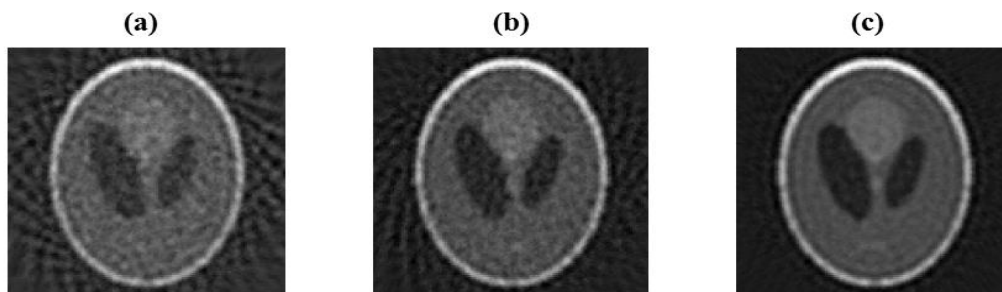
Figure 3.11. Reconstructed images of the modified Shepp-Logan phantom. The energy resolution of the detector is (a) 1000 eV, (b) 500 eV and (c) 100 eV. For this set of reconstructions, the detector pixel size is 2×2 mm^2. The dose limit is 12.8 mGy.

Figure 3.12(a)-(c) illustrates the MTF and demonstrates that the spatial resolution of the reconstructed images improves as the detector pixel size decreases reaching an optimum value for the 1×1 mm^2 detector. Figure 3.12(d)-(f) illustrates contrast values relative to the background for selected inserts of the phantom as a function of the detector pixel size. Figure 3.12(d), 3.12(e) and 3.12(f) correspond to 1000 eV, 500 eV and 100 eV energy resolutions respectively.

Figure 3.13 shows the PSNR and illustrates the trends in image quality improvement, with the maximum value corresponding to the optimum in terms of the overall quality. The curve indicates that a 2×2 mm^2 detector size is the best choice for the studied range of the detector sizes for all investigated energy resolutions.
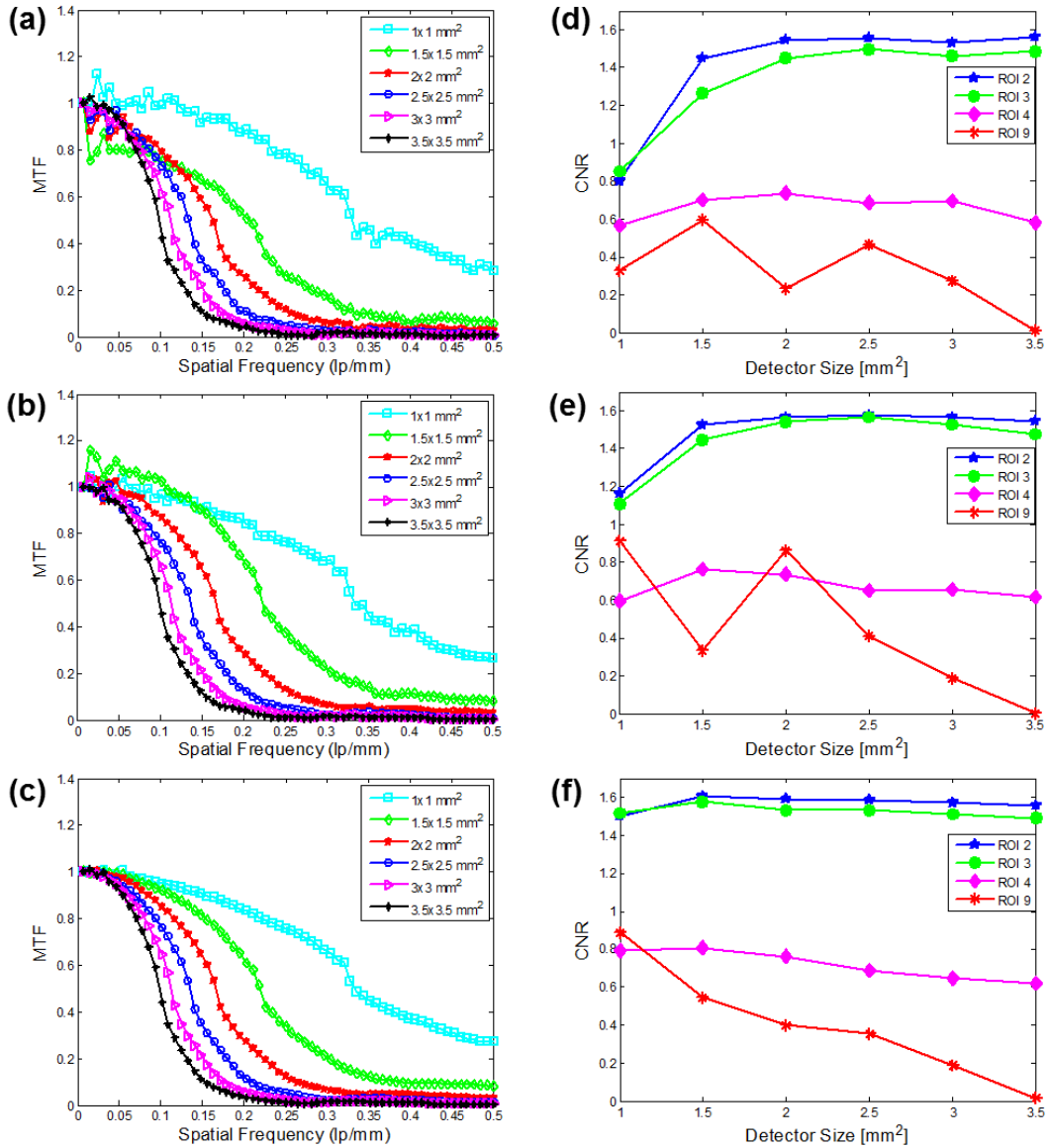
Figure 3.12. MTF of the imaging system at (a) 1000 eV, (b) 500 eV and (c) 100 eV detector energy resolutions, where each graph illustrates the improvement in MTF with a decrease in the detector pixel size.

The CNR for four ROIs defined for the modified Shepp-Logan phantom (see Figure 3.5 and Table 3.1) at (d) 1000 eV, (e) 500 eV and (f) 100 eV detector energy resolutions.
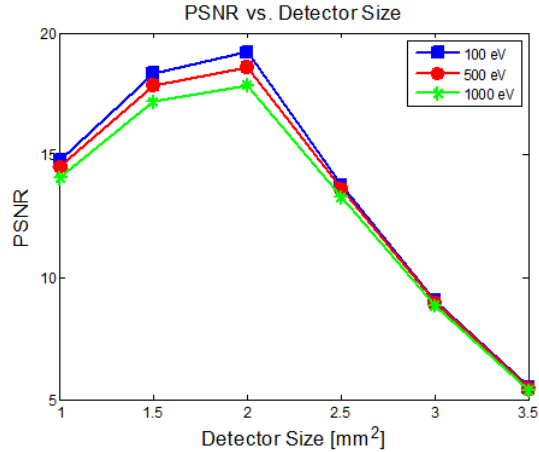
Figure 3.13. Dependence of PSNR on the detector pixel size for energy resolutions of 1000 eV, 500 eV and 100 eV. Detector pixel size increases from 1×1 mm^2 to 3.5×3.5 mm^2 with 0.5×0.5 mm^2 increments.

3.5. Discussion

3.5.1. Optimal detector size and energy resolution

The results demonstrate that it is possible to reconstruct images from scattered photons in the presence of noise (based on an acceptable dose for diagnostic imaging) while using attainable detector technology. An appropriate selection of detector size and energy resolution is required in order to optimize the image quality

As expected, the MTF of the imaging system improves as the detector pixel size decreases, irrespective of the energy resolution of the detector. Thus, to increase spatial resolution the size of the detector should be decreased, with the tradeoff being increase in the noise. Figure 3.12(d)-(f) illustrate that for an energy resolution of 1000 eV, the CNR for inserts ROI 2 and 3 initially increase with detector pixel size as the noise decreases and then stabilize for detectors larger than 1.5×1.5 mm^2. For this energy resolution, the CNR for the small insert (ROI 9) is always below that of ROI 4, which has the same inherent contrast, and decreases with increasing detector pixel size, which indicates that there is a loss of contrast due to blurring

associated both with the energy resolution and detector size. For the 500 eV energy resolution, the CNR for ROI 9 approaches that of ROI 4 for detector pixel sizes from 1×1 mm^2 to 2×2 mm^2, where the CNR is approximately independent of detector size. At 100 eV, the CNR for ROI 9 and ROI 4 only converge for the smallest detector size. In this case, the increase in spatial blurring associated with increasing detector size is more significant than the reduction in noise associated with an increase in photon count associated with larger detectors. Therefore, above 1.5×1.5 mm^2, with increase in the size detector does not significantly affect CNR.

The PSNR curve (Figure 3.13), which characterizes overall quality of the image, shows that, irrespective of energy resolution, the optimal detector pixel size is 2×2 mm^2. A 2×2 mm^2 detector pixel size at 500 eV energy resolution would appear to be the optimal combination for the defined dose, number of projections and imaging geometry.

3.5.2. The number of projections

Preliminary simulations indicate that a reasonable quality reconstructed image can be obtained using 36 projections while taking into account practical limitations such as the size of the generated data and the time required for the simulation.

Detailed investigation of the effect of the number of projections on the reconstructed image quality is described in Chapter 4.

3.5.3. Significance of the inclusion of the attenuation

The inclusion of attenuation into the simulation would reduce the single Compton scattering signal and increase the noise. However, the optimal values for the detector parameters are not strongly affected by the detected scattered photon fluence [66]. While the inclusion of attenuation into the reconstruction algorithm has yet to be investigated, we believe that the

incorporation of attenuation effects will not have a significant impact on the role that the detector size and energy resolution have on the reconstructed image quality.

3.5.4. Possible application of the technique

One of the potential applications of the described technique is dedicated breast CT. The ability to use scattered radiation to improve sensitivity and specificity of the modality would be of value [14, 18]. In breast CT, scatter is a significant contributor to the degradation of image quality. The scatter-to-primary ratio (SPR) in this modality ranges from 0.5 to 1 depending on the breast size and composition [21], and a SPR of 1.5 has been reported at the centre of a phantom [27]. As a result of the increased scatter, there is a decrease in CNR with a 15% decrease in CNR being found for 14 cm diameter breast [18]. Using an algorithm as described in this chapter to reconstruct images using both primary and scattered photons could be used to offset this effect and could increase the signal-to-noise ratio, improve contrast and allow recovery of the electron density of an object [49, 50].

3.6. Conclusions

The results of this work have shown that while limiting the dose to about 13mGy [84], the optimal detector pixel size for a Compton scatter reconstruction using 36 projections is in the range from 1.5×1.5 mm^2 to 2.5×2.5 mm^2. The best compromise between noise and blurring is achieved for a detector pixel size of 2×2 mm^2 with an energy resolution of approximately 500 eV. The results also demonstrate that the reconstructed image quality is more affected by a change in the detector size rather than by the energy resolution of the detector.

CHAPTER 4. The Impact of the Projection Number on Image Quality in Compton Scatter Tomography

4.1. Introduction

X-ray computed tomography (CT) is a widely used imaging modality, and there are ongoing efforts to increase the image quality and to reduce the dose [87]. Some work has been devoted to make better use of the scattered photons that are present in an x-ray system. The use of Compton scattered photons has been investigated for a range of imaging applications and in recent years there has been growing interest in Compton scatter tomography (CST) [49, 50, 65, 68, 69, 71]. If the detectors used in this imaging modality have sufficient energy and spatial resolution, and the photon count is high enough, CST can generate an image with a single projection. However, current detector technology does not have the spatial and energy resolution required to create an acceptable quality electron density image with only one projection. When reconstructing an image from a single projection using detectors with less than ideal energy and spatial resolution, the data space is sparsely populated. The lack of sampling can be overcome by using multi-projection Compton scatter tomography (MPCST), where the reconstructed images generated using Compton scattered photons obtained for each projection, are combined to create a single image of the electron density of the object [88]. To reiterate, the final image obtained in MPCST is a composite of the images acquired at each projection, even though under ideal conditions, one projection is sufficient to provide a full reconstruction.

4.1.1. Electron density image reconstruction using Compton scatter tomography

In x-ray Compton scatter imaging, scattered photons are used instead of primary photons for reconstruction and the resultant information is a map of the electron density, rather than the linear attenuation coefficient, of the imaged object. To reconstruct the origin of the Compton scattering event, an approach similar to filtered backprojection can be used. The backprojection of the scatter signal takes place over circular arcs that pass through the source, the detector and the scattering location.

The circular arcs are formed using the Compton equation (see Equation 3.1), which relates the energy of the incident photon to the energy of the scattered photon and the scattering angle. Knowledge of the locations of the source and detectors, as well as the incident and scattered photon energies, is presumed. Since all angles subtended by the same chord are equal, any point on the circular arc is a potential scattering location for a scattered photon of a particular energy.

Function recovery from integration over a curve was first introduced by Cormak [36, 37]. Kondic pointed out that the Compton equation can be used to place the scattering position along a circular path [52, 53], while Norton later introduced an analytical method which resembles filtered backprojection [54, 55].

4.1.2. Sampling requirement in CT and the implication for projection number in MPCST

The proposed CST geometry is based on a third generation CT system, with a fan-beam x-ray source and an 180^0 opposed detector array that rotates around the imaged object (Figure 4.1) [12, 13]. In conventional fan-beam geometry CT, the required number of projections is based on the Shannon-Nyquist sampling theory and streak artifacts occur in the reconstructed image, if this is violated [2, 38, 89]. In practice, the number of projections is typically obtained

from empirical measurements performed under practical conditions rather than from a strict application of the sampling theory. The number of projections used in commercial CT is usually of the order of 1000 per full 360^0 rotation [1, 2]. The requirements for the number of projections in CT is, however, not applicable to CST, as in this modality a good quality image can be produced with a single projection if the spatial and energy resolution of the detector is high enough [54, 55, 88].

Ideal conditions for CST require, amongst others, a point source of mono-energetic x-rays and a point detector with a high energy resolution. In practice, these conditions are not achieved, and the impact of the non-ideal features of the system on the reconstructed image quality must be investigated and reduced. Chapter 3 investigates the influence of the detector size and energy resolution for a system that modeled and simulated a 2D cross-sectional view of a breast CT geometry [88]. The system was adapted for scatter imaging and the investigation was performed using a fixed number of projections.

In MPCST, multiple images, each created from a single projection, are combined to create the final image. Increasing the number of projections increases the data space density, resulting in a potentially higher image quality. However, in a dose-constrained system, the signal-to-noise ratio of the image from a single projection decreases as the total number of projections is increased. For CST, the literature does not provide any guidance as to the optimal number of projections or even the method to determine this number. Optimization of the image acquisition conditions and an investigation of their tradeoffs are essential, and the current work examines the dependence of MPCST image quality as a function of projection number for various dose limits.

The results of this simulation study are not intended to be applied directly to clinical practice as a number of idealized conditions and simplifications are still assumed. The purpose of this work was to understand the impact of the number of projections on the image quality in order to establish a base from which corrections for multiple scatter and attenuation, as well as the impact of a poly-energetic source, could be investigated.
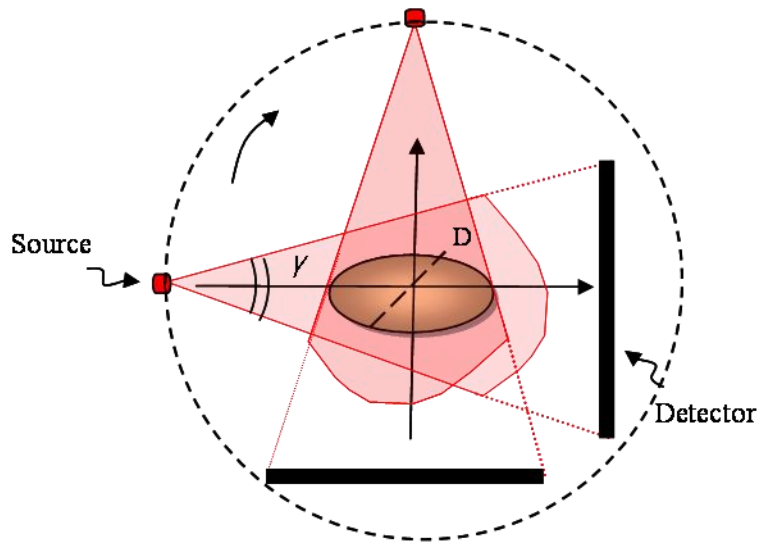
Figure 4.1. Schematic of traditional, third generation fan-beam CT where the source and detectors rotate around the isocenter of the system, and the object to be imaged is placed in the centre of the system.

4.2. Methods and materials

The goal of this work was to identify the optimal number of projections required to maximize the quality of the electron density image of the object for a particular fluence given a fixed detector energy and spatial resolution. Since a single projection can produce an adequate image given ideal conditions, we hypothesized that there would be an optimal projection number which would result from the tradeoff between improved sampling and the decrease in the signal-to-noise ratio per image as the projection number is increased [54, 88]. This investigation was performed using analytical simulations with the fluences that produce total doses that bracket the doses obtained in clinical breast CT. An extension of Norton's algorithm that uses filtered backprojection over circles, as used in Chapter 3, was employed to reconstruct the electron density images [54, 55, 88].

4.2.1. System configuration and image formation

The configuration of the simulated system illustrated in Figure 4.2 was the same as described in Chapter 3 [88]. The system was modeled by a fan-beam producing point x-ray source, and an array of energy sensitive photon counting detectors positioned along one edge of the fan-beam, in line with the source. The object being imaged was positioned at the isocenter of the system. A 55 keV mono-energetic photon beam and 2×2 mm^2 photon counting detectors with 500 eV energy resolution were used. The object imaged in the simulations was a modified Shepp-Logan phantom [82, 83, 88]. The electron density (ρ_e) values assigned to the digital phantom components reflected those found in human tissues. The distance from the source to the isocenter was 45 cm, the length of the array of the scatter detectors was 93.6 cm and the fan-beam angle was 31.8 degrees. Figure 3.5 depicts the phantom and Table 3.1 outlines the regions of interest (ROI) with the corresponding ρ_e values assigned to them. The analysis was described for four chosen ROIs of this phantom. The percentage differences between the electron densities of the depicted inserts relative to the electron density of the background were 400% for ROI 1, -100% for ROI 2 and 3 and 50% for ROI 4. Consequently, amongst considered inserts, the contrast was highest for ROI 1 and lowest for ROI 4.
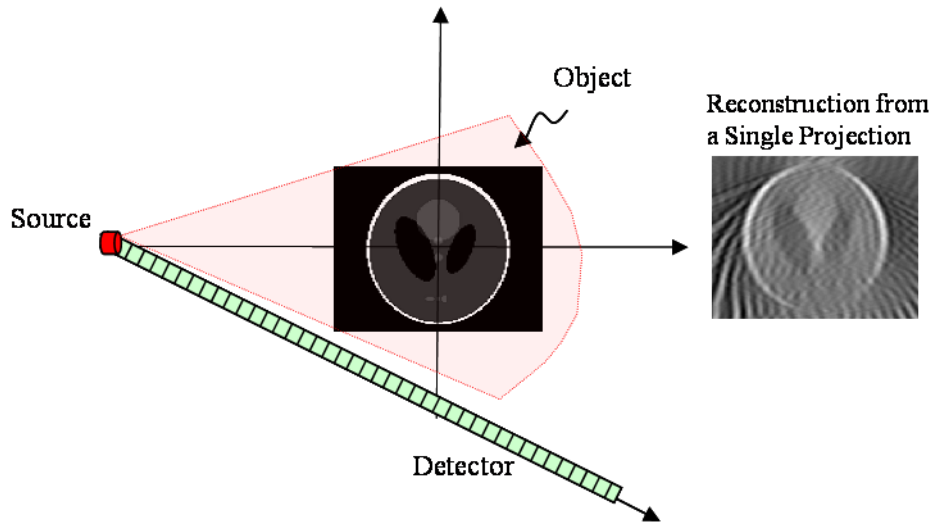
Figure 4.2. The figure illustrates the geometry of the simulated system. The system consisted of a 55 keV mono-energetic fan-beam x-ray source, the object being imaged (a modified Shepp-Logan phantom, see Figure 3.5) and photon counting energy sensitive detectors, placed in line with the source but just outside of the beam, for detecting the Compton scattered photons. The signal detected from a single projection can be reconstructed to generate an image with varying quality. The quality of each image will vary with the energy and spatial resolution of the detectors and the dose per projection.

Figure 4.3 schematically illustrates electron density image acquisition in MPCST. The non-ideal acquisition conditions result in each projection in the image sequence having less than adequate quality (Figure 4.3(a)). By combining these images (Figure 4.3(b)) the final image (Figure 4.3(c)) is obtained.
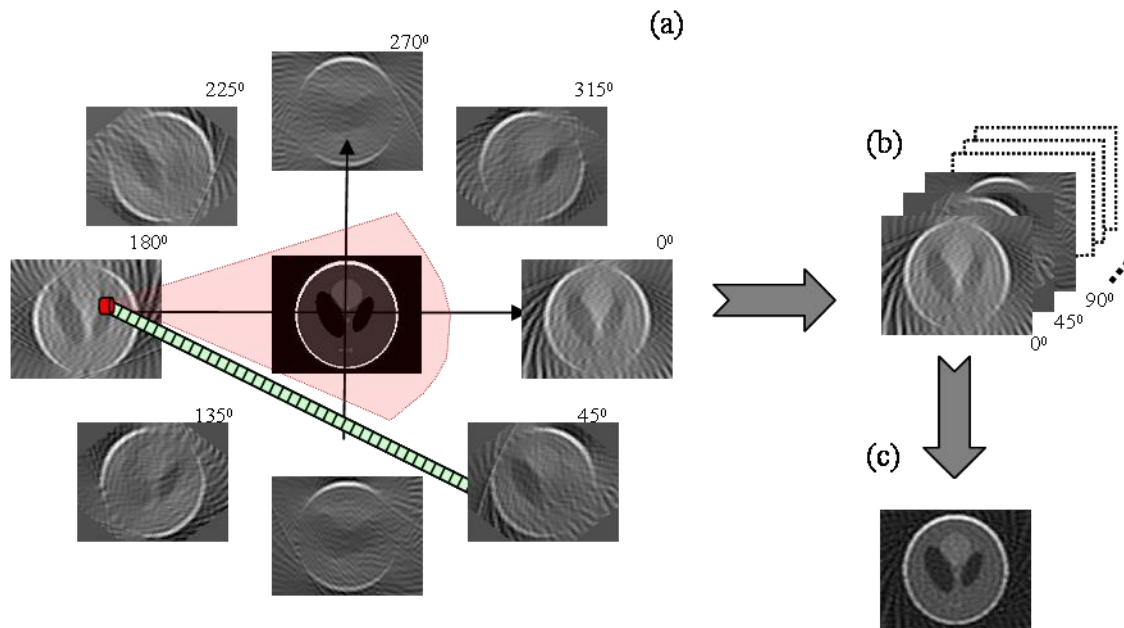
Figure 4.3. (a) This figure schematically illustrates the images reconstructed at eight different projection angles and (b) the sequence of reconstructed images acquired at each projection that are subsequently combined to obtain the final image (c).

4.2.2. Simulations

The simulations were designed to evaluate the competing impact of quantum noise per projection and sampling artifacts, as a function of dose and projection number. Noise in the projection data propagates into the reconstructed image, hence simulations were performed using four total incident fluences $(N_0) = 10^8$; 10^9; 10^{10} and 10^{11} [photons/mm^2]. The number of projections for each of these fluence levels was changed from 10 to 720 projections in increments of 10 projections acquired using 360^0 rotation with uniform equiangular spacing. The angular increment was decreased with an increase of the projection number while adjusting the number of incident photons per projection to keep the total photon count constant. The quantum noise per projection depends on the number of projections and the total incident photon fluence, and the signal-to-noise ratio (SNR) per projection varied over almost three orders of magnitude as shown in Figure 4.4. The projection data generated by the analytical model was randomized with Poisson noise [75].
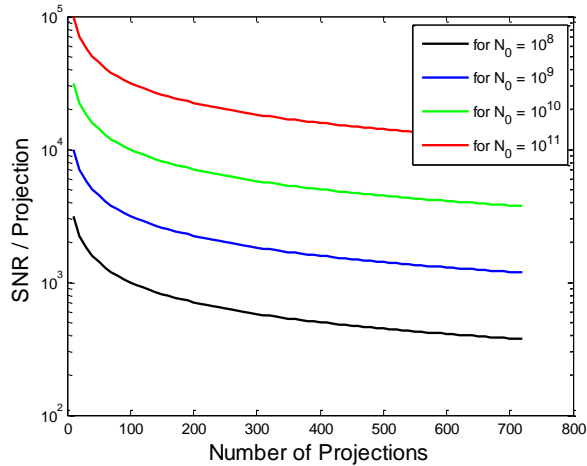
Figure 4.4. The signal-to-noise ratio per projection as a function of the number of projections while the total number of the incident photon fluence is constant ($N_0 = 10^8$; 10^9; 10^{10} and 10^{11} [photons/mm^2]).

4.2.3. Computational environment

The computational time is a function of the detector resolution and object grid size. The size of the modified Shepp-Logan phantom used in these simulations was 128×128 with a pixel size of 1×1 mm^2. The simulation and reconstruction algorithms were coded in MATLAB (The MathWorks, Inc., Natick, MA). A Dell PowerEdge R810 computer with four Intel Xeon E7-4860 2.26 GHz 10-core processors and 256 GB of RAM running SUSE Linux Enterprise 11.1 was used for all simulations. For a detector energy resolution of 500 eV and a detector size of 2×2 mm^2 the computational time per 360 projections was 12 minutes when using parallelization that calculates 12 projections concurrently.

4.2.4. Image quality assessment

The image quality, due to sampling as a function of the number of projections, was evaluated using noise free data. The analysis of the impact of the projection number on the production of artifacts was done using peak signal-to-noise ratio (PSNR) of noise free images obtained with one to 720 projections [90].

$$PSNR = 20 \ \log_{10} \frac{\max\left(S_{i,j}\right)}{\sqrt{MSE}} \qquad (4.1)$$

In Equation 4.1 the *MSE* (mean square error) is defined using the following expression:

$$MSE(S,R) = \frac{1}{NM} \sum_{i=1}^{N} \sum_{j=1}^{M} \left(S_{i,j} - R_{i,j}\right)^2$$

where *S* corresponds to the original image intensity, *R* corresponds to the reconstructed image intensity, *N*×*M* defines the size of the image, and *i* and *j* describe elements of the rows and columns of the image, respectively.

The reconstructed image quality was characterized by the contrast-to-noise ratio (CNR) and the modulation transfer function (MTF). The CNR, which was calculated for four selected inserts of the modified Shepp-Logan phantom, was defined by [75]:

$$CNR = \frac{\frac{1}{A}\sum_{a=1}^{A}\rho_e{}^a - \frac{1}{B}\sum_{b=1}^{B}\rho_e{}^b}{\sigma} \qquad (4.2)$$

where, $\frac{1}{A}\sum_{a=1}^{A}\rho_e{}^a$ is the mean electron density of the insert, $\frac{1}{B}\sum_{b=1}^{B}\rho_e{}^b$ is the mean electron density of the background and σ is the standard deviation of the background.

Additional simulations to define MTF of the system were performed to evaluate the spatial resolution and to determine how it related to the number of projections [75]. For this set of simulations, a point phantom located at the isocenter of the system was used. The system configuration was the same as that used for the tests involving the modified Shepp-Logan phantom. The MTF was obtained by calculating Fourier transform of the line spread function (LSF), which was generated by radially averaging the point spread function (PSF) of the simulated point object.

4.3. Results and discussions

Figure 4.5 illustrates the electron density images reconstructed from the noise free data generated using one to eight projections. This figure shows the impact that the artifacts have on the image quality. It demonstrates that there is not a visually significant improvement in the image quality above the reconstruction obtained using four projections.

Figure 4.6 illustrates the increase in the PSNR due to a decrease in artifacts as the number of projections increases from one to 720. The figure shows that for a given energy and spatial

resolution of the detector (500 eV and 2×2 mm^2, respectively), and for noise free conditions, the number of projections above which the PSNR curve does not exhibit noticeable change lays within the range from 4 to 30 projections.

Figure 4.7 shows reconstructed images of the modified Shepp-Logan phantom, obtained using different number of projections. The number of incident photons used in these simulations is 10^{10}. The improvement in the image quality as a function of projection number is visually apparent, with improvement in the quality becoming subtle as the number of projections exceeds 360. For a small number of projections (first row), low contrast objects e.g. ROI 4 are overwhelmed by noise and are not visible. As the number of projections reaches 360, the contrast-to-noise ratio has improved to the point where ROI 4 is visible. This visual assessment complies with the image quality metric illustrated in Figure 4.9(c) that corresponds to the N$_0$ used to generate Figure 4.7. Figure 4.9 shows a shallow gradient of the CNR curve above 360 projections.

Figure 4.8 provides visual perception of the correlation between the quality of the reconstruction and the number of projections, and fluence.

Figure 4.9(a-d) illustrates CNR distributions for four ROIs of the phantom as a function of the number of projections for four different N$_0$, which increased by three orders of magnitude from 10^8 (Figure 4.9(a)) to 10^{11} (Figure 4.9(d)). The CNR increases as the number of projection increases for all four ROIs and all considered fluences. After a certain point further increase in the number of projections, which increases the noise per projection, does not demonstrate an effect on the CNR. The increase in the CNR, as a function of projection number, is due to a decrease in the noise in the final image. The increase in the noise per projection is removed because of the averaging of images acquired at different projections. The noise in the CNR values depends on the number of incident photons. For low doses, high noise overshadows the contrast and small structures in the image become hard to distinguish. For high incident fluences, the noise per projection is low. Consequently, the improvement in the image quality in terms of the

noise reveals for a lower number of projections used. Figure 4.9(e-h) shows CNR curves for four different fluences, as a function of the projection number for four defined ROIs. Figure 4.9(e)-(h) correspond to ROI 1 – ROI 4 respectively.

Figure 4.10 illustrates the CNR distributions for four ROIs of the phantom as a function of the number of projections and incident fluence. It combines the information depicted by Figure 10 and presents it into 3D format.

Figure 4.11(a) shows the plot of the MTFs for a different number of projections (4, 8, 15, 45 and 90 projections) using 2×2 mm^2 size detectors with an energy resolution of 500 eV. Figure 4.11(b) illustrates the MTFs for single projections using detectors that have different energy resolutions and sizes (5eV & 1.125×1.125mm^2; 50eV & 1.5×1.5mm^2 and 500eV & 2×2mm^2 respectively). Figure 4.11(a) indicates that the spatial resolution is independent of the number of projections while Figure 4.11(b) demonstrates that as the energy and spatial resolution of the detector decreases causing decrease in the sampling, the spatial resolution of the image decreases.
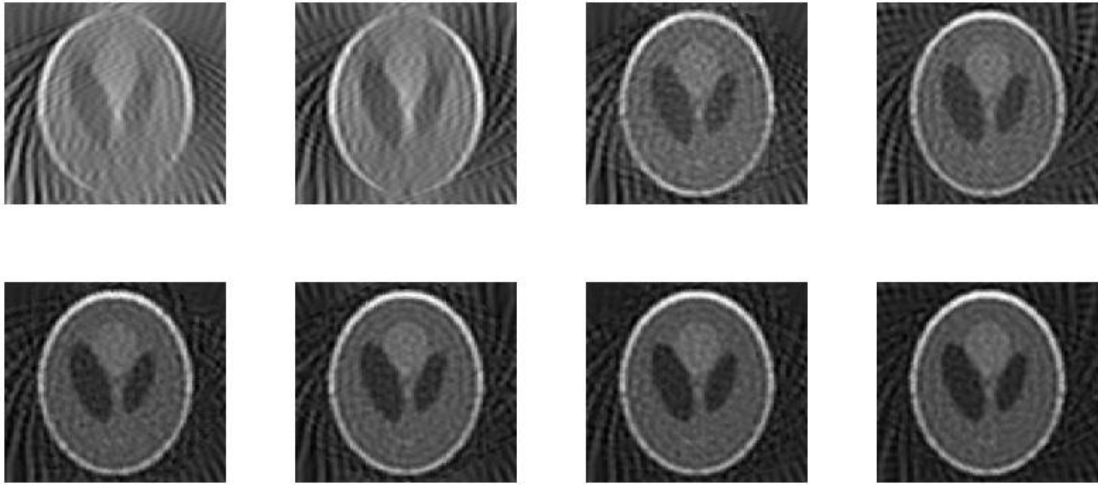
Figure 4.5. Electron density images reconstructed from noise free data generated using 1, 2, 3, 4, 5, 6, 7 and 8 projections, from top left to the bottom right.
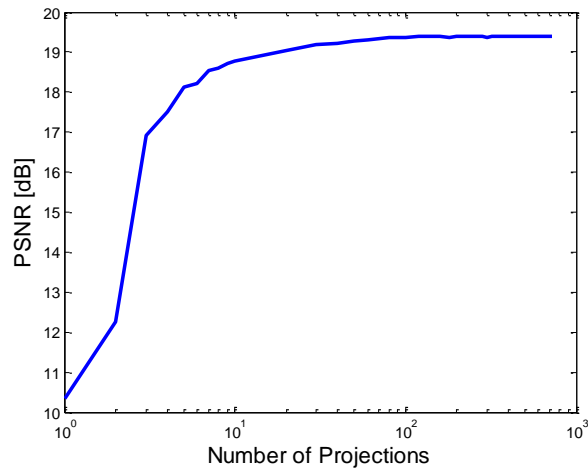
Figure 4.6. PSNR as a function of the number of projections for the reconstructions performed from noise free data. This graph illustrates the change in the PSNR due to a change in sampling reducing the artifacts as the number of projections increases from one to 720.
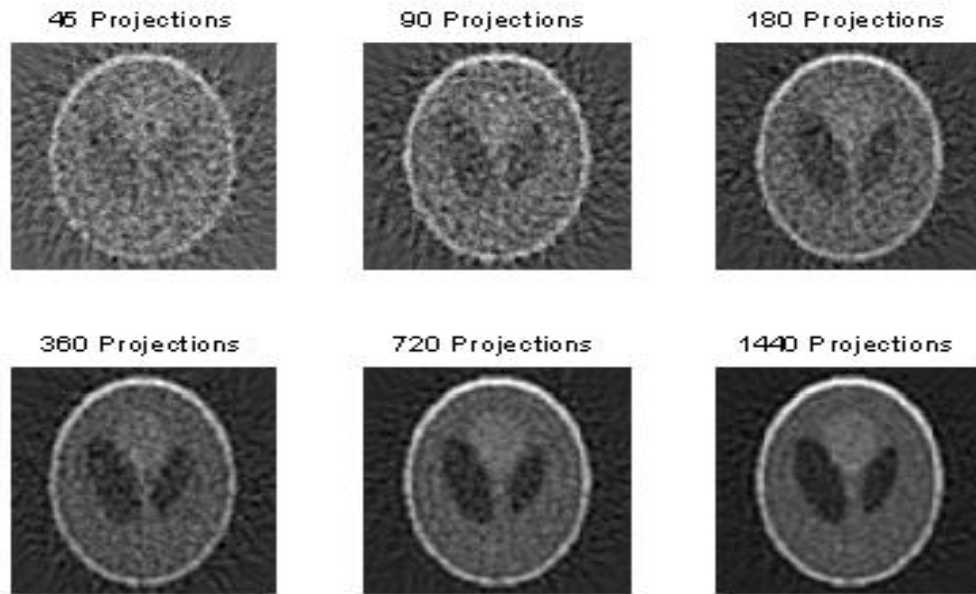
Figure 4.7. Set of the reconstructed images obtained using different number of projections. The number of projections used to obtain final image increases from 45 (top left) to 1440 (bottom right). The number of incident photons used in this case was 10^{10}.
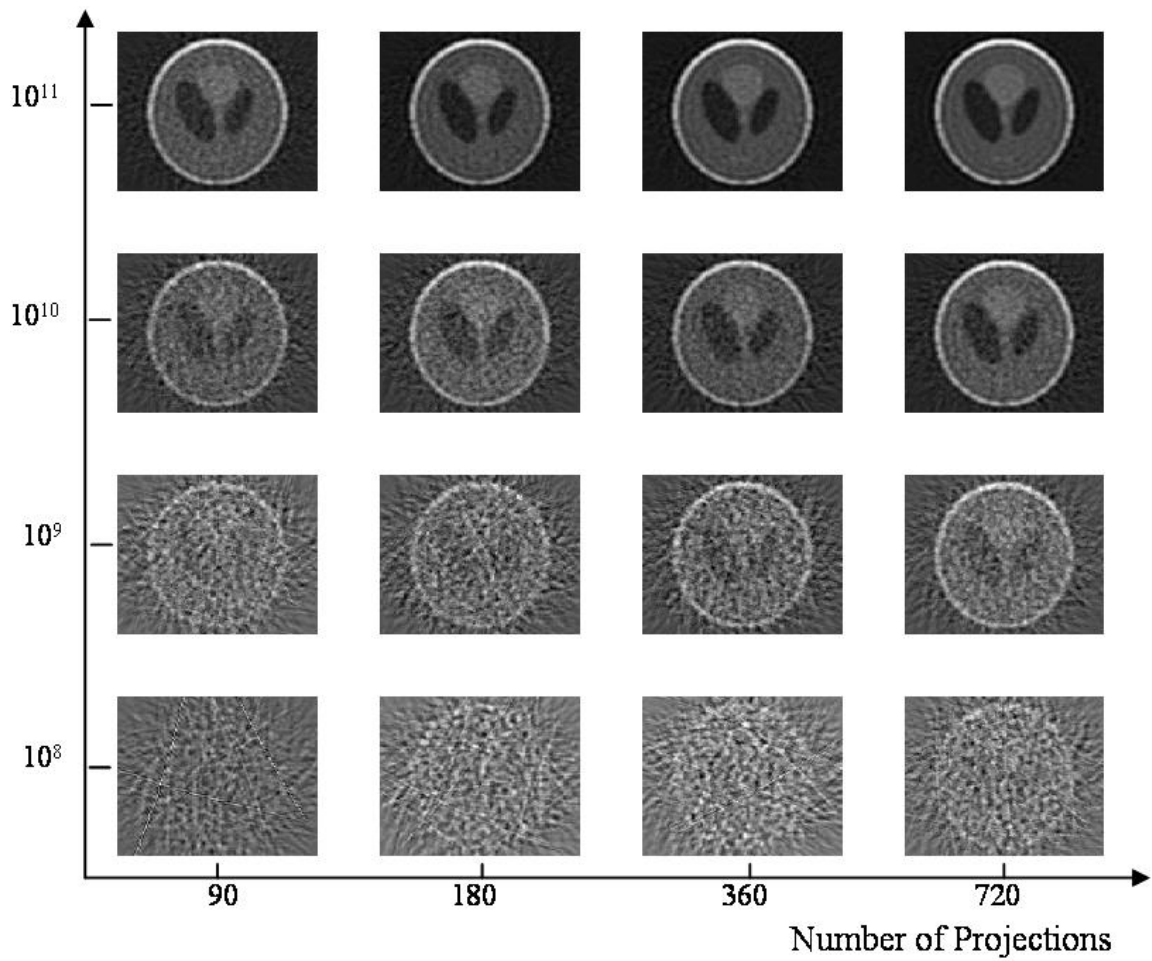
Figure 4.8. Reconstructed images obtained using different number of projections (90, 180, 360 and 720 from left to right) for four different fluences that increase by the order of magnitude ($N_0 = 10^8$; 10^9; 10^{10} and 10^{11} from bottom to top).
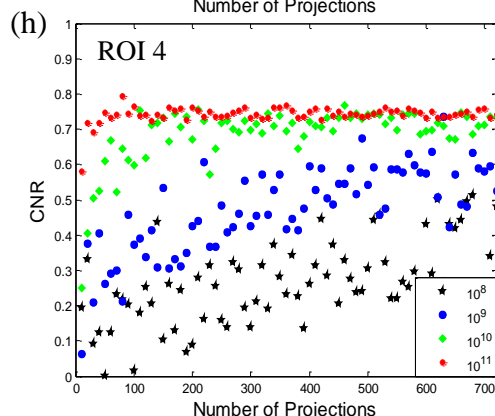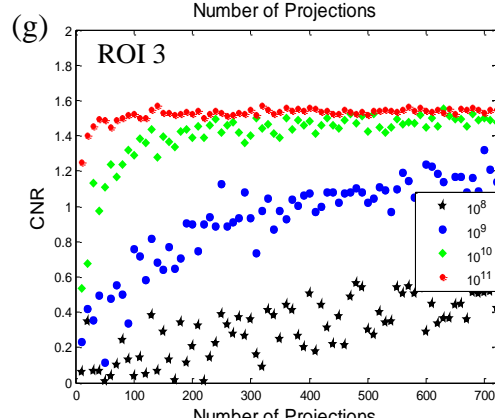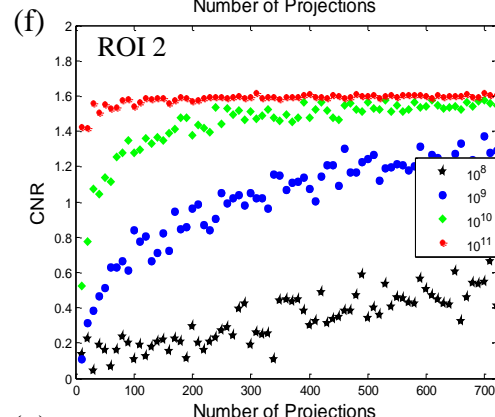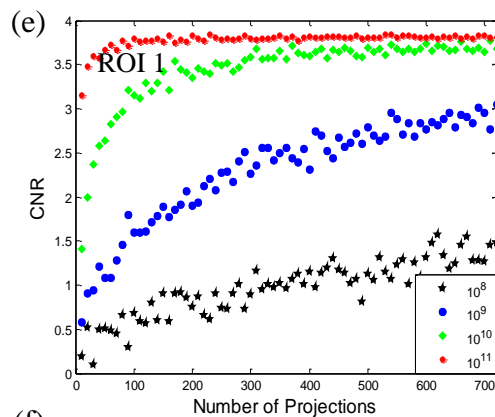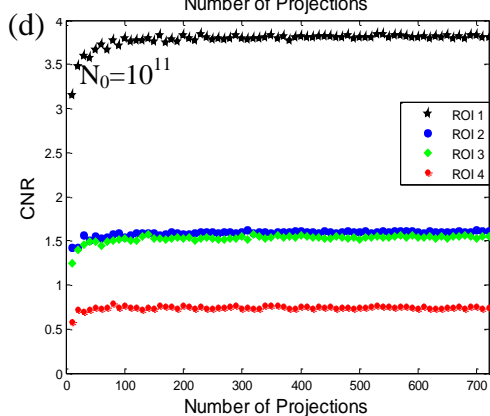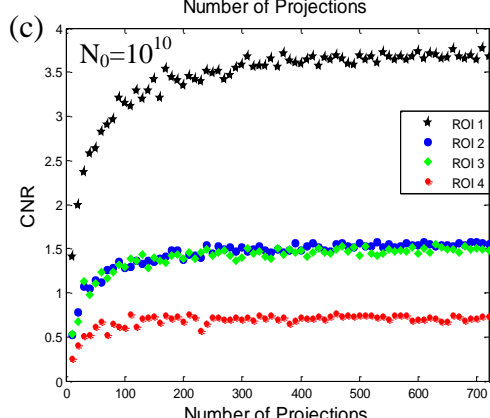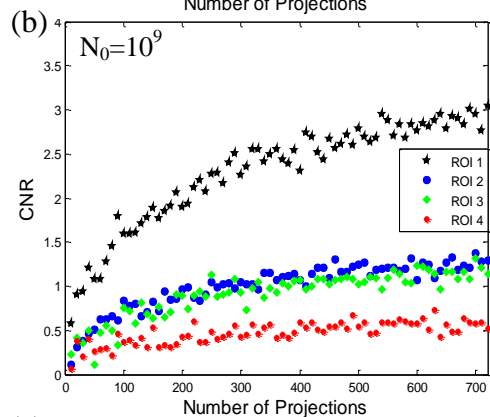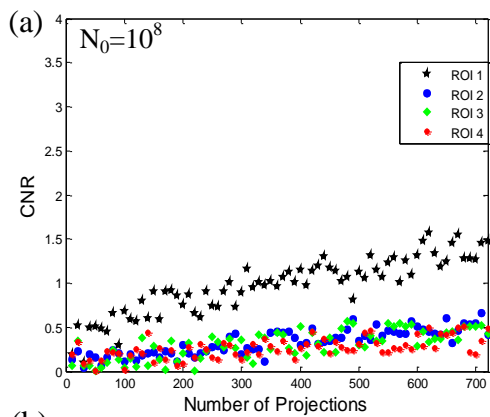
Figure 4.9. CNR distributions for four different N_0 values that increase in steps of the order of magnitude from top (a) $N_0 = 10^8$ to bottom (d) $N_0 = 10^{11}$, for four ROIs of the modified Shepp-Logan phantom (see Figure 3.5) illustrated as a function of the number of projections. (e)-(h) display CNR for ROI 1, ROI 2, ROI 3 and ROI 4 respectively, for four different fluences as a function of the projection number.
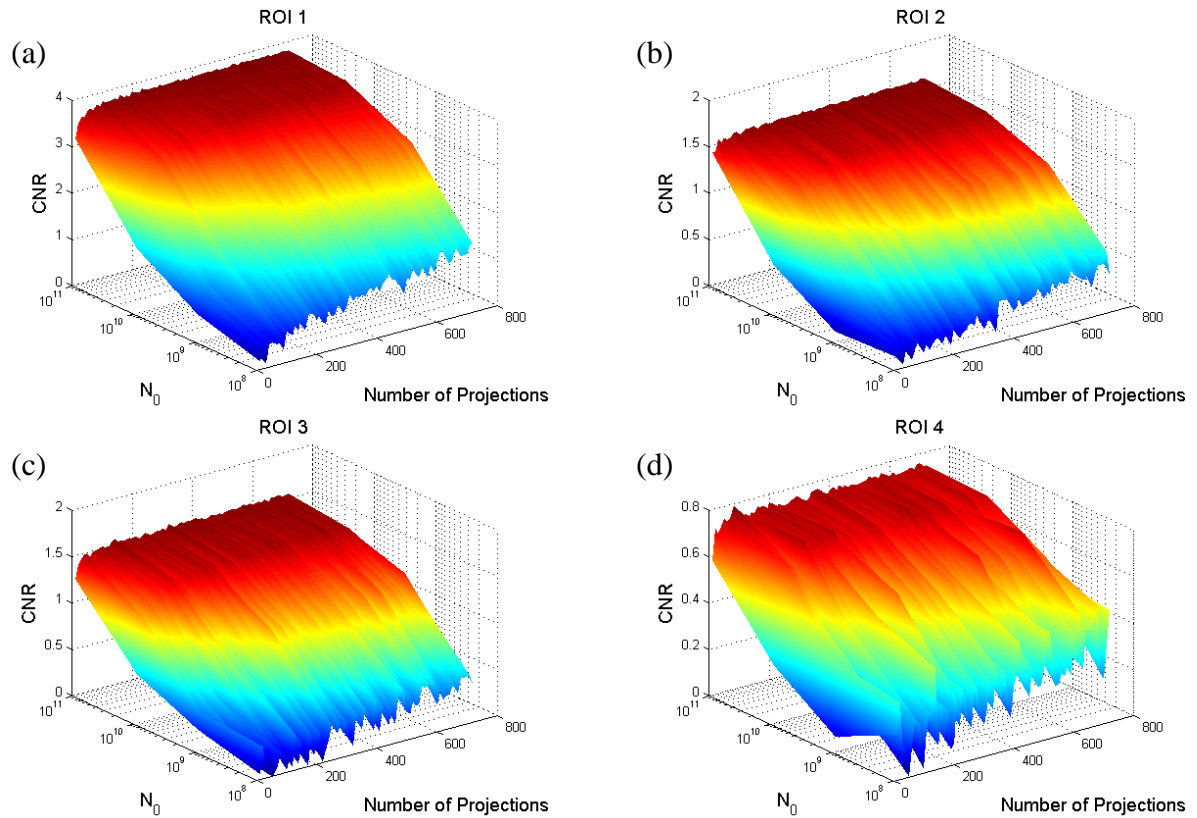
Figure 4.10. CNR distributions for four ROIs of the modified Shepp-Logan phantom illustrated as a function of the fluence and number of projections. The range of considered projection number is from 10 to 720 with an increment of 10 projections. The number of incident photons considered are $N_0 = 10^8$; 10^9; 10^{10} and 10^{11}. Note the different scale for different materials.
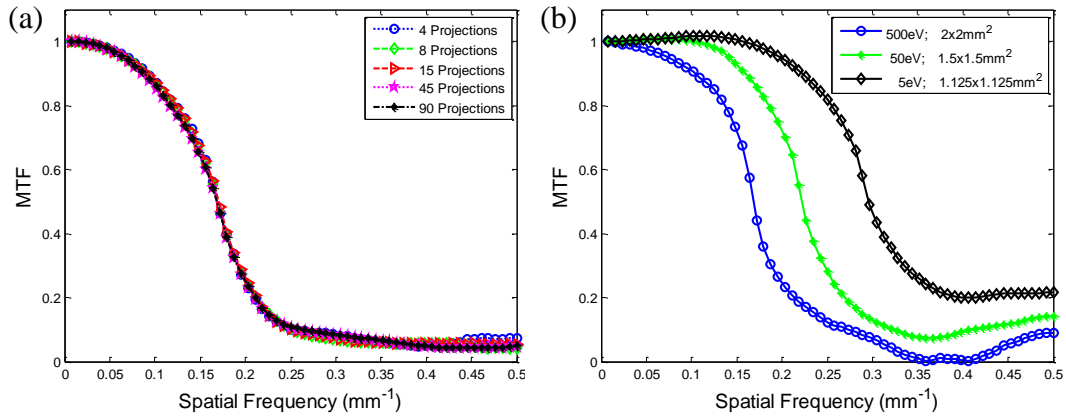
Figure 4.11. (a) MTFs for 4, 8, 15, 45 and 90 projections using detectors with energy resolution of 500eV and size of $2\times2mm^2$. (b) Plot of the MTFs for a single projection. The plot illustrates cases, when the energy resolution and size of the detectors are 5eV and $1.125\times1.125mm^2$; 50eV and $1.5\times1.5mm^2$ and 500eV and $2\times2mm^2$. Note, due to the Nyquist theory the limiting resolution for the $1.125\times1.125mm^2$ detector is $f_N = 0.44$; for $1.5\times1.5mm^2$ detector $f_N = 0.33$; for $2\times2mm^2$ detector $f_N = 0.25$.

4.4. Conclusions

We investigated the influence of the number of projections for the system configuration that corresponds to the 2D cross-sectional view of the breast CT set-up adapted to detect scatter signal. This study was performed using analytical simulations while limiting the total dose. The results show that the increase of the projection number gradually improves the contrast with this dependence being a function of fluence. The number of projections required to approach the asymptotic maximum contrast decreases as the fluence increases. Moreover, within the range of the investigated projection number (from one to 720), while increasing the number of projections, even for the lowest dose value, the CNR increases even though the number of photons per projection decreases.

Furthermore, it was illustrated that for MPCST with a detector energy resolution of 500 eV and a size of 2×2 mm^2, a low noise and artifact image can be obtained with a small number of projections provided the incident fluence is high enough. When the fluence approaches a noise free scenario, the number of projections required is in the range from 4 to 30.

The results also suggest that increasing the number of projections increases the contrast-to-noise ratio but not the spatial resolution. In MPCST the spatial resolution of the image is mainly defined by the number of detectors [88]. Thus, an improvement in spatial resolution is obtained by increasing the sampling within a projection, rather than by increasing the number of projections. The detector energy resolution also contributes to the image quality but this is constrained, as it is not possible to improve the energy resolution beyond that of the theoretical limit of the detector.

CHAPTER 5. Summary and Future work

5.1. Summary

X-ray based medical examination is a crucial part of diagnosis and consequently treatment. The x-ray imaging process is inevitably accompanied by scattered radiation that, if not corrected for, introduces degradation in the reconstructed image quality leading to potential misinterpretation of the results. An optimal x-ray imaging would combine information from the primary signal as well as from the scatter signal. Information extracted from the scattering signal would facilitate complete characterization of the imaged object composition [45]. Thus, the capture and use of the scattering signal is of interest.

The goal of this thesis was to explore feasibility of the image formation from Compton scattering signal in practicable fan-beam breast CT geometry. We investigated a number of parameters affecting reconstructed electron density image quality (detector size, detector energy resolution, number of projections), their tradeoffs and described the methods for the image quality improvement. When detector spatial and energy resolution is ideal ρ_e images can be obtained using a single projection. These ρ_e images can be reconstructed using filtered backprojection over isogonic curves. Non-ideal specifications of the detector lead to image quality degradation, to compensate for this current work introduces multi-projection Compton scatter tomography (MPCST). The design of the system investigated in the current work is modeled after a 2D cross-sectional view of a breast CT geometry. In the proposed system, the image is acquired while a fan-beam producing x-ray source and an array of energy sensitive photon counting detectors located alongside of the edge of the incident beam rotate around the object while acquiring scattering data.

Chapter 3: The reconstructed electron density image quality is sensitive to the detector size and energy resolution, which contribute to the blurring and noise in the image. Chapter 3, which was published in the *Journal of X-Ray Science and Technology* [88], evaluates the optimal values of the detector parameters through analytical simulations of the transverse slice of the dedicated breast CT system geometry. This study introduces a spectroscopic x-ray tomography technique, which uses multiple projections to reconstruct electron density images by backprojecting scattered photons over isogonic curves. The reconstruction can be obtained using a single projection yet its quality degrades as the acquisition conditions (i.e. detector size and energy resolution) deviate from the ideal. The reconstruction quality becomes inconsistent throughout the image due to the data under-sampling caused by the finite resolution of the detector. The extension to the multi-projection mode effectively fills-in the missing data space and improves the ability to reconstruct an object. In this study, investigating the optimal values for the detector specifications, a fixed number of projections (36 projections) was used. This work demonstrates the possibility to obtain images in the presence of noise.

Chapter 4: In principle, the availability of high-resolution energy discriminating photon counting detectors should make it possible to use Compton scattered photons to improve the diagnostic capability of CT. With high spatial and energy resolution detectors, CST images of adequate quality can be obtained even with a single projection. However, the limitations of realistic detectors require multiple projections for good quality images. The relationship between the number of projections used for reconstruction and the reconstructed image quality obtained for conventional CT does not necessarily apply to MPCST. Chapter 4 investigates the dependence of the reconstructed image quality on the number of projections for MPCST. Analytical simulations and reconstruction were used to evaluate the contrast and spatial resolution for images obtained with one to 720 projections. CNR and MTF demonstrated that the contrast increases monotonically with the number of projections, while spatial resolution was independent

of the number of projections. The contrast initially increases rapidly with the projection number, becoming more gradual as the number of projections increase, with the dependence being a function of fluence. The number of projections required to asymptotically approach the maximum contrast decreases as the fluence increases, with no sign of an optimal value for the range of fluences and projections investigated. For the range of the investigated number of projections, an increase in the number of projections increases the CNR even though the number of photons per projection decreases.

The major contribution of this work is to provide an insight into the behavior of the reconstructed electron density image quality, associated with energy and spatial resolution of the detector and the number of projections. A decrease in the detector size increases spatial resolution in the reconstructed image with the tradeoff being an increase in the noise. We established that introducing a multi-projection approach could offset the downfall associated with the decrease in the detector size. Our work indicates that, within the premise of the defined system geometry, investigated range of the projection angles and detector spatial and energy resolution, the increase in the noise can be compensated for by increasing the number projections.

While there remain a number of issues to be overcome before the considered approach becomes clinically feasible, we believe MPCST may facilitate the improvement of sensitivity and specificity of CT imaging. The work provided in this thesis will allow further investigation of the issues associated with this approach, including the effects of multiple scatter and attenuation.

5.2. Assumptions

A number of assumptions were made in the process of the electron density image recovery from the Compton scattering signal. These assumptions include the availability of a mono-energetic source, discarding of the signal contaminating multiple scatter and the attenuation undergone by photons.

5.2.1. Mono-energetic source

The current work uses a mono-energetic incident beam, which commonly is considered to be an assumption. Recent studies on the benefits and feasibility of a quasi-monoenergetic beam offer options for a suitable mono-energetic source. Quasi-monoenergetic beams with an energy bandwidth ranging from 0.2 to 2.5 keV can be generated in a number of different ways. They can be obtained using x-ray tubes with heavy filtration. For example, via simulation we found that, for the tube operating at 90 kVp with tungsten target using a filter consisting of 0.5 mm tungsten and 1.2 mm erbium, a beam with a mean energy of 55 keV and a full width at half maximum (FWHM) of 2.5 keV can be obtained (Figure 5.1) [91, 92]. Alyassin et al. propose using [241]Am, a 59.5 keV γ-ray nuclide source, to produce medical radiographic images comparable to x-ray images [93]. Mono-energetic radiation can be produced using a synchrotron [94, 95] or a more affordable laser-driven x-ray source [96].
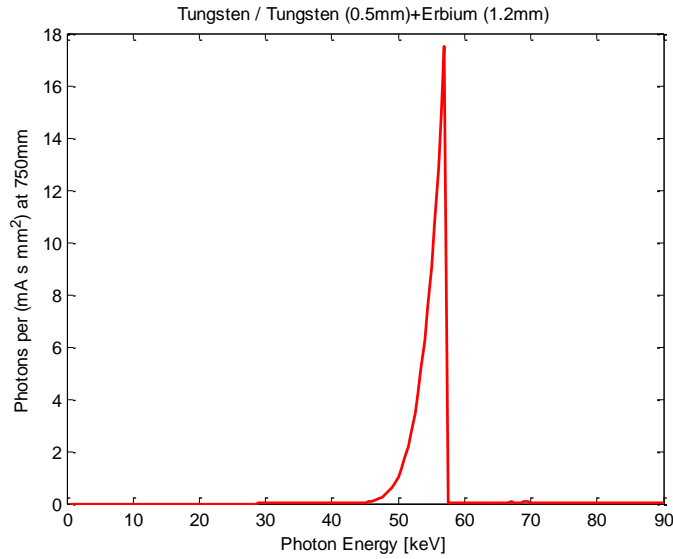
Figure 5.1. Incident x-ray beam spectrum simulated using IRSU-78 software.

The precision of the reconstruction from the scattered photons relates to the x-ray spectral width. With the increase of the x-ray spectral width, the spatial resolution of the reconstructed image decreases. Figure 5.2 shows a backprojection path, which is a circular arc for the ideal case but broadens as the energy bandwidth increases. This is similar to the shortcoming associated with the finite energy resolution detectors, and this shortcoming can be addressed by using multiple projections.

$$E_s = \frac{E_0 + \Delta E_0}{1 + \frac{E_0 + \Delta E_0}{m_0 c^2} \cdot (1 - \cos \theta')}$$

$$E_s = \frac{E_0 - \Delta E_0}{1 + \frac{E_0 - \Delta E_0}{m_0 c^2} \cdot (1 - \cos \theta')}$$
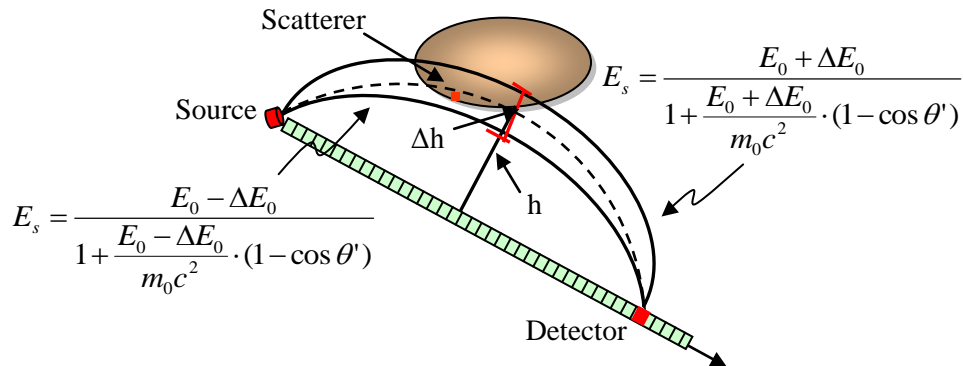
Figure 5.2. Illustration of the effect that a source/detector having a small energy bandwidth has on the scattering location defining isogonic curve.

5.3. Future work

5.3.1. Handling multiple scatter

The presence of multiple scatter results in an increase in the Compton scattering signal, which leads to the overestimation of the electron density, while the reverse is true for attenuation. The use of the relationship between the energy of the Compton scattering signal and the scattering angle, for the purpose of the localization of the scattering, becomes inaccurate. Thus, the consideration should be given to the issue of multiple scatter and the development of the model to predict and account for it. To address the problem of multiple scatter, Alpuche Aviles et al. [67] have shown that it is possible to reconstruct an object from multiple scattering using a signal scatter model. While qualitatively correct, the image overestimated the electron densities. Subsequent work by the same group achieved correct reconstructed values by using an empirical correction to the single scattering model [61]. As a result, an improvement in the reconstructed image contrast was obtained. A similar approach could be taken in our work. Furthermore, since our approach has an advantage of providing scattering signal energy, this information can be used as an initial phase for the signal correction by rejecting photons that have undergone multiple scattering.

5.3.2. Handling attenuation

The main challenge of Compton scatter imaging is addressing the issue associated with attenuation. In Lale's work [3], which provided the impetus for Compton scatter imaging for medical application, the issue caused by the attenuation effect was avoided by using a high-energy beam. Clarke and Van Dyk [97] suggested use of both primary and scattered γ-ray signal in order to facilitate correction for attenuation. In subsequent years, a number of publications

describing attenuation correction methods were presented. These techniques include iterative methods and attenuation estimation directly from CT data [63-65, 67, 98].

Throughout this work, the scattering signal has been characterized using expression (2.8), which does not account for attenuation undergone by photons. In practice, attenuation should be accounted for as the detected signal undergoes attenuation along the path from the source to the scattering location (R) and from that location to the detector (R') (Figure 5.3). Considering these attenuation factors (AF), the expression for the scatter signal should be modified accordingly:

$$N_{sc} = N_0 \cdot \exp\left(-\int_{source}^{scatterer} \mu(E_0, R)dR\right) \cdot \rho_e \cdot dv \cdot \frac{d\sigma}{d\Omega} \cdot d\Omega \cdot \exp\left(-\int_{scatterer}^{detector} \mu(E_S, R')dR'\right) \qquad (5.1)$$
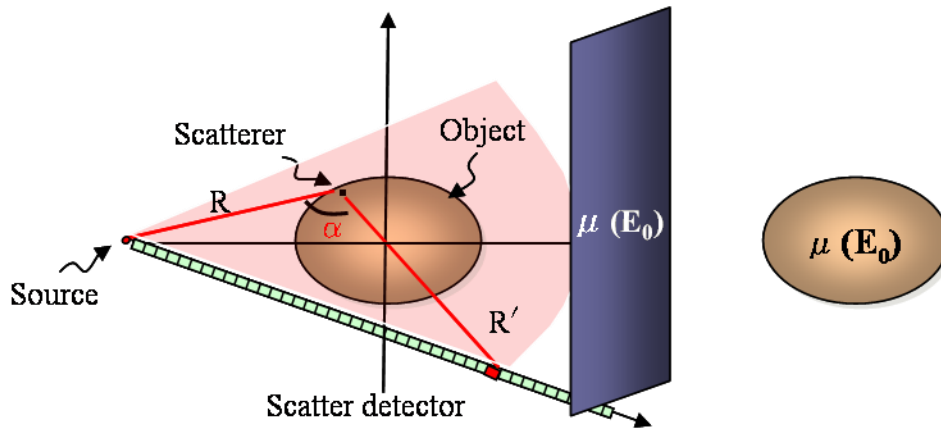
Figure 5.3. Illustration of the CT/CST system set-up outlining the paths from the source to the scatterer (R) and from that scatterer to the detector (R').

75

Hence, in order to obtain synthetic projection data that accounts for attenuation undergone by the photons, we incorporated *AF*s into the analytical data acquisition process. The inclusion of the *AF*s into forward data was done using Siddon's algorithm, which enables the calculation of the radiological path [99]. For this simulation, the inserts of the phantom were assigned electron density values of: cortical bone (skeletal), blood (whole), adipose, glandular, muscle (skeletal) and vacuum. The values for listed materials were taken from ICRU report 44 [100]. The values of mass linear attenuation coefficients at particular energy were defined from Hubble and Seltzer [85].

Figure 5.4 illustrates the scattering data (c-sinograms) that incorporates attenuation undergone by the photons and the reconstruction created without applying correction for the attenuation. The data was generated for 100 eV energy and a 1×1 mm^2 spatial resolution photon counting detector, for 360 equiangular projections. From the image illustrating the reconstruction (Figure 5.4(b)), it is visually evident that the original object is restored though with suboptimal quality. Visual evaluation of the image shows a decrease in the image quality towards the edge of the phantom, due to the geometry of the set-up. When acquiring an image from a single projection, the signal that originates from the portion of the phantom that is located distally to the array of the scatter detectors (e.g. scatterer at Figure 5.3), will be heavily attenuated. Moreover, a part of this signal might not even reach the detector array resulting in a lower quality relative to the rest of the image. When expanding the approach to multiple projections, the described effect extends leading to the lower quality towards the edge of the phantom. This effect is more explicit when analyzing profiles through the reconstructed image (Figure 5.5(b)). One can see an inverse cupping artifact induced by the underestimated values at the edge and overestimated values towards the center of the phantom.
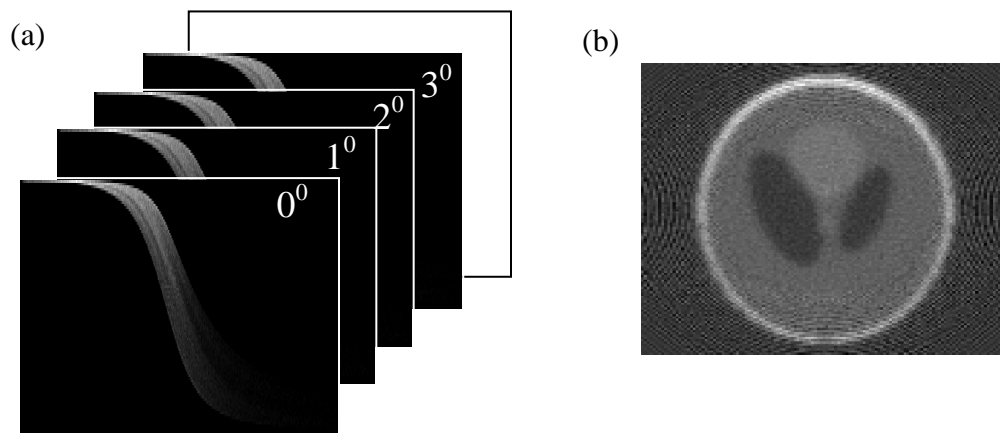
Figure 5.4. (a) Illustration of the scatter data, i.e. c-sinograms for the first four projections out of 360 equiangular projections that were simulated for modified Shepp-Logan phantom. These data incorporate pre and post scatter attenuation factors and are acquired using a detector with 100 eV energy and 1×1 mm^2 spatial resolution. (b) Reconstructed electron density image obtained using the attenuated scattering data, with no correction for the attenuation in the reconstruction process.
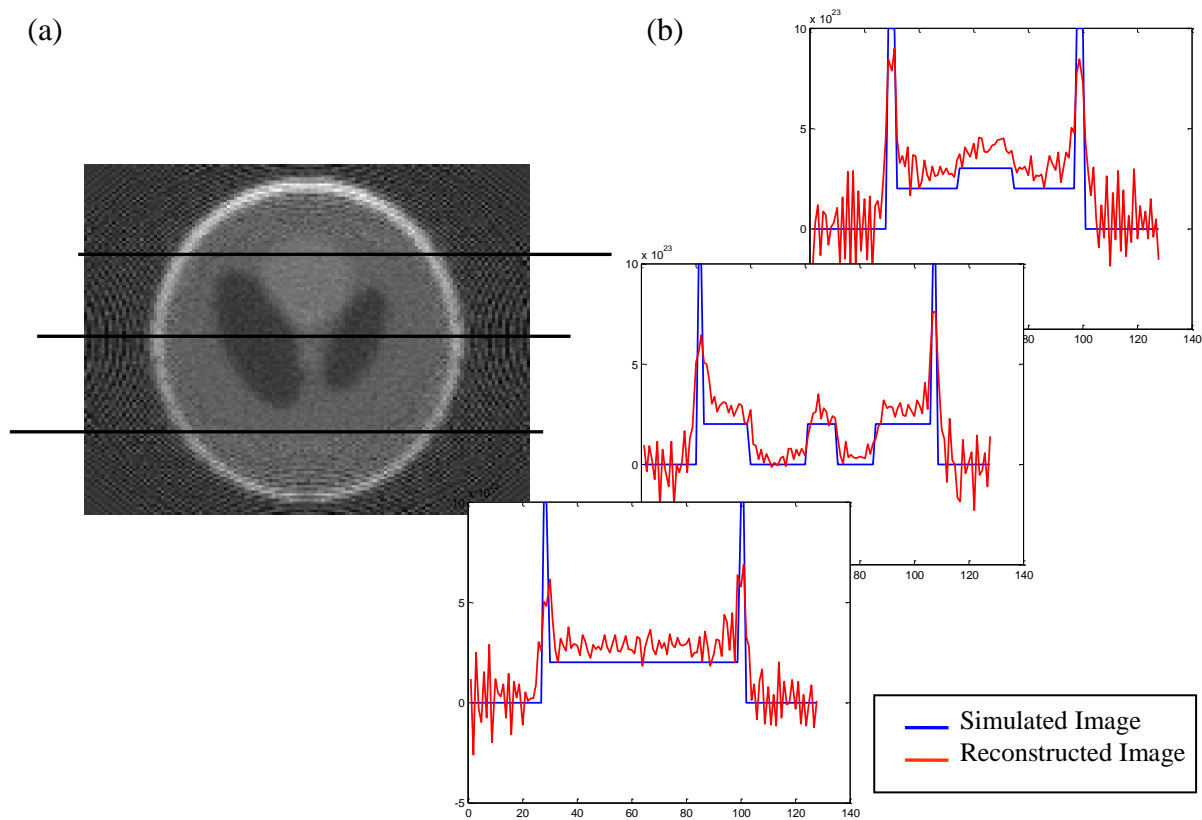
Figure 5.5. (a) Reconstructed image from attenuated scattering data with no correction for the attenuation. (b) Profiles through the original and reconstructed images at three locations highlighted on the Figure (a).

For the electron density (ρ_e) image recovery, a method to incorporate *AF*s into the inversion of the scatter signal should be established. An outline of the solution to this problem, which is to be addressed in future work, is described below. Figure 5.6 illustrates this process. The suggested approach for characterization of the attenuation factors is based on one of the methods presented in the literature for handling attenuation [67].

The Compton scatter tomography technique, presented in this thesis, ultimately will be a constituent of transmission CT. Hence, CT/CST system will produce images from primary and from scattering signal. The primary signal results in the attenuation map ($\mu(E_0)$), whereas the scattering signal leads to the electron density distribution of the imaged object. To integrate attenuation correction into the electron density map formation, the attenuation obtained from the transmission signal can be used (Figure 5.6). This attenuation map will facilitate an initial estimate for the electron density values via normalization to water $\left(\mu(E_0) \times \dfrac{\rho_e^{water}}{\mu(E_0)^{water}} \right)$. *AF*s can be defined from the ratio of the scattering signal defined in the absence of attenuation (Equation 2.8) and the one that accounts for the attenuation (Equation 5.1). Subsequently, these approximate *AF*s will be used to adjust the scattered data from CST, to generate the ρ_e image (Figure 5.6 (ii)). This ρ_e image (Figure 5.6 (ii)) is to be compared with the first estimate of the electron density distribution within the object (Figure 5.6 (i)), which is obtained from the transmission data. For the next recurrence of this process the ρ_e image obtained from the scattered data, which is corrected by the *AF*s, will become the new reference image. The iteration process will continue until the convergence is reached [67].
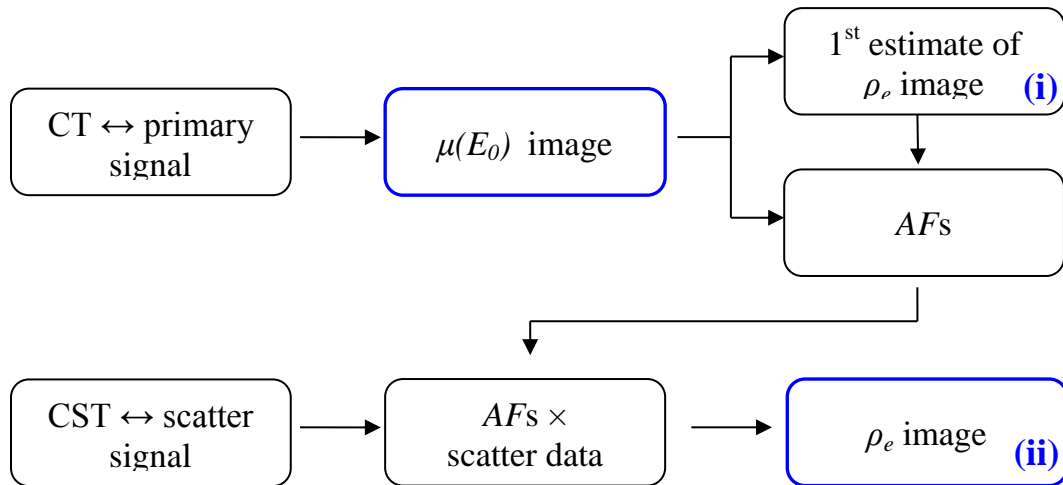
Figure 5.6. Flowchart outlining the process of the integration of the attenuation factors into the electron density image formation in CT/CST system.

References

1.   J. Hsieh, *Computed Tomography Principles, Design, Artifacts and Recent Advances*. second ed. 2009: SPIE and John Wiley & Sons, Inc. p. 61-69, 72, 127, 214-226, 232.

2.   A.C. Kak and M. Slaney, *Principles of Computerized Tomographic Imaging*. 2001, Piladelphia: Society for Industrial and Applied Mathematics. p. 56-60, 63-68, 107, 177-201.

3.   P.G. Lale, *The examination of internal tissues using gamma-ray scatter with a possible extension to megavoltage radiography*. Phys. Med. Biol., 1959. **4**: p. 159-67.

4.   F.T. Farmer and M.P. Collins, *A New Approach to the Determination of Anatomical Cross-sections of the Body by Compton Scattering of Gamma-Rays*. Phys Med Biol, 1971. **16**: p. 577-586.

5.   A. Jemal, et al., *Global cancer statistics*. CA: A Cancer Journal for Clinicians, 2011. **61**(2): p. 69-90.

6.   International Agency for Research on Cancer. *GLOBOCAN 2012: Estimated Cancer Incidence, Mortality and Prevalence Worldwide in 2012; January 29, 2014; Available at: www.iarc.fr*.

7.   Am.CancerSoc., *Cancer Facts & Figures 2012*. Atlanta, GA: Am. Cancer Soc., 2012.

8.   M.J. Yaffe and J.G. Mainprize, *Risk of Radiation-induced Breast Cancer from Mammographic Screening*. Radiology, 2011. **258**: p. 98-108.

9.   C.H. Lee, *Screening mammography: proven benefit, continued controversy*. Radiol Clin N Am, 2002. **40**: p. 395-407.

10.   S. Woloshin and L.M. Schwartz, *The Benefits and Harms of Mammography Screening Understanding the Trade-offs*. JAMA, 2010. **303**: p. 164-165.

11.   O.W. Brawley, *Risk-Based Mammography Screening: An Effort to Maximize the Benefits and Minimize the Harms*. Ann Intern Med., 2012. **156**: p. 662-663.

12.   W.A. Kalender, *CT: the unexpected evolution of an imaging modality.* Eur. Radiol., 2005. **15** p. D21–D24.

13.   W.A. Kalender, *X-ray computed tomography.* Phys. Med. Biol., 2006. **51**(13): p. R29-R43.

14.   J.S. Glick, *Breast CT.* Annual Review of Biomedical Engineering, 2007. **9**(1): p. 501-526.

15.   C.H. Chang, *Computed Tomography of the Breast.* Radiology, 1977. **124**(3): p. 827 - 829.

16.   J.M. Boone, et al., *Dedicated Breast CT: Radiation Dose and Image Quality Evaluation.* Radiology, 2001. **221**(3): p. 657-667.

17.   B. Chen and R. Ning, *Cone-beam volume CT breast imaging: Feasibility study.* Medical Physics, 2002. **29**(5): p. 755-770.

18.   T.G. Schmidt, *Dedicated Breast CT: Current Status and New Directions.* Current Medical Imaging Reviews, 2010: p. 61-71.

19.   J.M. Boone, et al., *Computed Tomography for Imaging the Breast.* Journal of Mammary Gland Biology and Neoplasia, 2006. **11**(2): p. 103-111.

20.   K.K. Lindfors, et al., *Dedicated Breast CT: Initial Clinical Experience.* Radiology, 2008. **246**(3): p. 725-733.

21.   A.L.C. Kwan, J.M. Boone, and N. Shah, *Evaluation of x-ray scatter properties in a dedicated cone-beam breast CT scanner.* Medical Physics, 2005. **32**(9): p. 2967.

22.   R.C. Chen, et al., *Measurement of the linear attenuation coefficients of breast tissues by synchrotron radiation computed tomography.* Phys. Med. Biol., 2010. **55**: p. 4993–5005.

23.   M. Torikoshi, et al., *Electron density measurement with dual-energy x-ray CT using synchrotron radiation.* Phys. Med. Biol., 2003. **48**: p. 673–685.

24.   J.S. Al-Bahri and N.M. Spyrou, *Electron Density of Normal and Pathological Breast Tissues using a Compton Scattering Technique.* Appl. Radiat. Isot., 1998. **49**(12): p. 1677-1684.

25.   E.A. Ryan, M.J. Farquharson, and D.M. Flinton, *The use of Compton scattering to differentiate between classifications of normal and diseased breast tissue.* Phys. Med. Biol., 2005. **50**: p. 3337-3348.

26.   D.J. Brenner and E.J. Hall, *Computed Tomography - An Increasing Source of Radiation Exposure.* N Engl J Med, 2007. **257**: p. 2277-2284.

27.   G. Mettivier, et al., *Evaluation of Scattering in Cone-Beam Breast Computed Tomography: A Monte Carlo and Experimental Phantom Study.* IEEE Trans. Nucl. Sci., 2010. **57**: p. 2510-2517.

28.   J.H. Siewerdsen, et al., *The influence of antiscatter grids on soft-tissue detectability in cone-beam computed tomography with flat-panel detectors.* Medical Physics, 2004. **31**(12): p. 3506.

29.   E.P. Ruhrnschopf and K. Klingenbeck, *A general framework and review of scatter correction methods in x-ray cone-beam computerized tomography. Part 1: Scatter compensation approaches.* Medical Physics, 2011. **38**(7): p. 4296.

30.   R.D. Speller and J.A. Horrocks, *Photon scattering - a 'new' source of information in medicine and biology?* Phys. Med. Biol., 1991. **36**: p. 1-6.

31.   F.H. Attix, *Introduction to radiological physics and radiation dosimetry*. 1986: John Wiley & Sons, Inc. p.124-156.

32.   G. Harding, *On the Sensitivity and Application Possibilities of a Novel Compton Scatter Imaging System.* IEEE Transactions on Nuclear Science, 1982. **NS-29**: p. 1260-1265.

33.   W.A. Kalender, *Computed Tomography Fundamentals, System Technology, Image Quality, Applications*. 2nd ed. 2005, Erlangen: Publics Corporate Publishing.

34.   T.M. Buzug, *Computed Tomography From Photon Statistics to Modern Cone-Beam CT*. 2008: Springer-Verlag Berlin Heidelberg.

35. X. Pan, E. Y. Sidky, and M. Vannier, *Why do commercial CT scanners still employ traditional, filtered back-projection for image reconstruction?* Inverse Problems, 2009. **25**(123009).

36. A.M. Cormack, *Representation of a function by its line integrals with some radiological applications.* J. Appl. Phys., 1963. **34**: p. 2722-2727.

37. A.M. Cormack, *The Radon transform on a family of curves in the plane.* Proc. Am. Math. Soc., 1981. **83**: p. 325-330.

38. P.M. Joseph and R.A. Schulz, *View sampling requirements in fan beam computed tomography.* Med. Phys., 1980. **7**(6): p. 692-702.

39. D. Fleischmann and F.E. Boas, *Computed tomography—old ideas and new technology.* Eur Radiol, 2011. **21**: p. 510-517.

40. HighTechRochester. [cited 2014 May 21]; http://htr.org/koning-corporation].

41. A.M. O'Connell, *The Evolution and Future of Dedicated Breast CT.* Breast Diseases: A Year Book Quarterly, 2012. **23**(2): p. 131-133.

42. A. Karellas and S. Vedantham, *Breast cancer imaging: A perspective for the next decade.* Med. Phys., 2008. **35**(11): p. 4878-4897.

43. C.H.J. Chang, et al., *Computed Tomographic Evaluation of the Breast.* Am J Roentgenol, 1978. **131**: p. 459-464.

44. M.J. Yaffe and P.C. Johns, *Scattered Radiation in Diagnostic Radiology: Magnitudes, Effects, and Methods of Reduction.* J. Appl. Photog. Eng., 1983. **9**: p. 184-195.

45. C. Theodorakou and M.J. Farquharson, *Human soft tissue analysis using x-ray or gamma-ray techniques.* Phys. Med. Biol., 2008: p. R111–R149.

46. S.H. Evans, et al., *Measurement of small-angle photon scattering for some breast tissues and tissue substitute materials.* Phys. Med. Biol., 1991. **36**(1): p. 7-18.

47. U. Kleuker, et al., *Feasibility study of x-ray diffraction computed tomography for medical imaging.* Phys. Med. Biol., 1998. **43**: p. 2911-2923.

48.   G. Harding, J. Kosanetzky, and U. Neitzel, *Elastic scatter computed tomography.* Phys. Med. Biol., 1985. **30**(2): p. 183-186.

49.   G. Harding, *Inelastic Photon Scattering: Effects and Applications in Biomedical Science and Industry.* Radiat. Phys. Chem., 1997. **50**: p. 91-111.

50.   G. Harding and E. Harding, *Compton scatter imaging: A tool for historical exploration.* Applied Radiation and Isotopes, 2010. **68**(6): p. 993-1005.

51.   F.A. Balogun and P.E. Cruvinel, *Compton scattering tomography in soil compaction study.* Nuclear Instruments and Methods in Physics Research Section A: Accelerators, Spectrometers, Detectors and Associated Equipment, 2003. **505**(1-2): p. 502-507.

52.   N. Kondic, *Density Field Determination by an External Stationary Radiation Source Using a Kernel Technique*, in *ASME Winter Annual Meeting, Symposium on Polyphase Flow Measurements*. 1978: San Francisco, CA.

53.   N.N. Kondic, A.M.Jacobs, and D. Ebert, *Three dimensional density field determination by external stationary detectors and gamma sources using selective scattering*, in *Proc. 2nd Int. Topical Mtg. On Nuc. React. Therm.-Hydr*. 1983. p. 1443-1455.

54.   S.J. Norton, *Compton scattering tomography.* J. Appl. Phys., 1994. **76**: p. 2007-2015.

55.   S.J. Norton, *Compton scattering tomography*. 1995, United States Patent.

56.   J. Wang, Z. Chi, and Y. Wang, *Analytic reconstruction of Compton scattering tomography.* J. Appl. Phys., 1999. **86**: p. 1693-1698.

57.   R. Guzzardi and G. Licitra, *A critical review of Compton imaging.* Crit. Rev. Biomed. Eng., 1988. **15**(3): p. 237-268.

58.   E.M.A. Hussein, *On the intricacy of imaging with incoherently-scattered radiation.* Nuclear Instruments and Methods in Physics Research Section B: Beam Interactions with Materials and Atoms, 2007. **263**(1): p. 27-31.

59.   J.J. Battista, L.W. Santon, and M.J. Bronskill, *Compton scatter imaging of transverse sections: corrections for multiple scatter and attenuation.* Phys Med Biol, 1977. **22**: p. 229–244.

60.   G. Harding and R. Tischler, *Dual-energy Compton scatter tomography.* Phys Med Biol, 1986. **31**: p. 477-489.

61.   J.E. Alpuche Aviles, et al., *A 1st generation scatter CT algorithm for electron density breast imaging which accounts for bound incoherent, coherent and multiple scatter: A Monte Carlo study.* Journal of X-Ray Science and Technology, 2011. **19**: p. 477–499.

62.   R.D. Speller and J.A. Horrocks, *A Monte Carlo study of multiple scatter effects in Compton scatter densitometry.* Med. Phys., 1988. **17**: p. 707-712.

63.   P. Busono and E.M. Hussein, *Algorithms for density and composition discrimination imaging for fourth generation CT systems.* Phys Med Biol, 1999. **44**: p. 1455-1477.

64.   N.V. Arendtsz and E.M.A. Hussein, *Energy spectral Compton scatter imaging. I. Theory and mathematics.* IEEE Transactions on Nuclear Science, 1995. **42**: p. 2155–2165.

65.   T.T. Truong and M.K. Nguyen. *Recent Developments on Compton Scatter Tomography: Theory and Numerical Simulations*. Numerical Simulation - From Theory to Industry 2012   2012-09-19;   Available   from: http://www.intechopen.com/books/export/citation/EndNote/numerical-simulation-from-theory-to-industry/recent-developments-on-compton-scatter-tomography-theory-and-numerical-simulations.

66.   T. Chighvinadze and S. Pistorius. *The effect of fluence and detector size on image quality in multi-projection Compton scatter tomography*. in *COMP*. 2012. Halifax, Canada.

67.   J.E. Alpuche Aviles, et al., *A novel hybrid reconstruction algorithm for first generation incoherent scatter CT (ISCT) of large objects with potential medical imaging applications.* Journal of X-Ray Science and Technology, 2011. **19**: p. 35–56.

68.   M.K. Nguyen and T.T. Truong, *Inversion of a new circular-arc Radon transform for Compton scattering tomography.* Inverse Problems, 2010. **26**(6): p. 065005.

69.   T.T. Truong and M.K. Nguyen, *Radon transforms on generalized Cormack's curves and a new Compton scatter tomography modality.* Inverse Problems, 2011. **27**(12): p. 125001.

70. G. Rigaud, M. Nguyen, and A.K. Louis, *Novel numerical inversions of two circular-arc radon transforms in Compton scattering tomography.* Inverse Problems in Science and Engineering, 2012. **20**(6): p. 809-839.

71. G. Rigaud, M.K. Nguyen, and A.K. Louis, *Modeling and simulation results on a new Compton scattering tomography modality.* Simulation Modelling Practice and Theory, 2013. **33**: p. 28-44.

72. T. Chighvinadze and S. Pistorius. *WE-G-211-03: Multiple Projection Compton Scatter Tomography*. in *COMP/AAPM*. 2011. Vancouver, Canada.

73. R.M. Eisberg and R. Resnick, *Quantum Physics of Atoms, Molecules, Solids, Nuclei, and Particles*. Second ed. 1985, New York: Wiley & Sons. p. 90-95.

74. F. Natterer, *The Mathematics of Computerized Tomography*. 2001, Philadelphia: Society for Industrial and Applied Mathematics. p. 158-178.

75. J.T. Bushberg, et al., *The essential physics of medical imaging*. 2002, Philadelphia: Lippincott Williams & Wilkins. p. 261-262, 270-283.

76. D.A. Chesler, S.J. Riederer, and N.J. Pele, *Noise Due to Photon Counting Statistics in computed X-Ray Tomography.* J Comput Assist Tomogr, 1977. **1**(1): p. 64-74.

77. P.M. Shikhaliev and S.G. Fritz, *Photon counting spectral CT versus conventional CT: comparative evaluation for breast imaging application.* Phys. Med. Biol., 2011. **56**(7): p. 1905-1930.

78. J.S. Yadav, S. Savitri, and J.P. Malkar, *Near room temperature X-ray and -ray spectroscopic detectors for future space experiments.* Nuclear Instruments and Methods in Physics Research Section A: Accelerators, Spectrometers, Detectors and Associated Equipment, 2005. **552**(3): p. 399-408.

79. A. Meuris, et al., *Caliste 64, a new CdTe micro-camera for hard X-ray spectro-imaging.* Nuclear Instruments and Methods in Physics Research Section A: Accelerators, Spectrometers, Detectors and Associated Equipment, 2009. **610**(1): p. 154-157.

80. Z. Wang and A.C. Bovik, *A Universal Image Quality Index.* IEEE Signal Processing Letters, 2002. **9**: p. 81-84.

81.   A. Wegener, et al., *Effects of fixed-rate CT projection data compression on perceived and measured CT image quality.* SPIE Medical Imaging, 2010. **7627**: p. 76270G-76270G-12.

82.   J.M. Boone, N. Shah, and T.R. Nelson, *A comprehensive analysis of DgN(CT) coefficients for pendant-geometry cone-beam breast computed tomography.* Medical Physics, 2004. **31**(2): p. 226-235.

83.   L.A. Shepp and B.F. Logan, *The Fourier reconstruction of a head section.* IEEE Trans. Nucl. Sci., 1974. **NS-21**: p. 21-43.

84.   A. O'Connell, et al., *Cone-Beam CT for Breast Imaging: Radiation Dose, Breast Coverage, and Image Quality.* American Journal of Roentgenology, 2010. **195**(2): p. 496-509.

85.   J.H. Hubbell and S.M. Seltzer, *Tables of X-Ray Mass Attenuation Coefficients and Mass Energy-Absorption Coefficients*. [Access date: 2008; 2013], http://www.nist.gov/pml/data/xraycoef/index.cfm. National Institute of Standards and Technology (NIST).

86.   P. Gravel, G. Beaudoin, and J.A. DeGuise, *A Method for Modeling Noise in Medical Images.* IEEE Transactions on Medical Imaging, 2004. **23**(10): p. 1221-1232.

87.   J.T. Payne, *CT Radiation Dose and Image Quality.* Radiol Clin N Am, 2005(43): p. 953-962.

88.   T. Chighvinadze and S. Pistorius, *The Effect of Detector Size and Energy Resolution on Image Quality in Multi-Projection Compton Scatter Tomography.* Journal of X-Ray Science and Technology, 2014. **22**: p. 113-128.

89.   P.M. Joseph, *Radiology of the skull and brain*, ed. T.H. Newton and D.G.Potts. Vol. 5. 1980: C.V. Mosby Company. p. 3956-3967.

90.   Q. Huynh-Thu and M. Ghanbari, *Scope of validity of PSNR in image/video quality assessment.* Electronics Letters, 2008. **44**(13): p. 800-801.

91.   K. Cranley, et al., *Catalogue of Diagnostic Spectra and Other Data.* (The Institute of Physics and Engineering in Medicine, York, U.K.), 1997.

92.   T. Chighvinadze and S. Pistorius. *Evaluation of Spectroscopic Compton Tomography Approach at 55 keV*. in *COMP*. 2009. Victoria, Canada.

93.   A.M. Alyassin, et al., *Feasibility study of gamma-ray medical radiography.* Applied Radiation and Isotopes, 2013. **72**: p. 16-29.

94.   K. Landheer and P.C. Johns, *Synchrotron-based coherent scatter x-ray projection imaging using an array of monoenergetic pencil beams.* Review of Scientific Instruments, 2012. **83**(9): p. 095114.

95.   R. Baba, et al., *Improving image quality of synchrotron CT by scattered X-ray correction.* Journal of Physics: Conference Series, 2013. **425**: p. 192010.

96.   K. Achterhold, et al., *Monochromatic computed tomography with a compact laser-driven X-ray source.* Sci Rep. 3: 1313 | DOI: 10.1038/srep01313, 2013.

97.   R.L. Clarke and G. Van Dyk, *A new method for measurement of bone mineral content using both transmitted and scattered beams of gamma-rays.* Phys. Med. Biol., 1973. **18**(4): p. 532-539.

98.   T.H. Prettyman, et al., *A combined transmission and scattering tomographic approach to composition and density imaging.* Appl. Radiat. Isot., 1993. **4**: p. 1327-1341.

99.   R.L. Siddon, *Fast calculation of the exact radiological path for a three-dimensional CT array.* Med. Phys., 1985. **12**(2): p. 252-255.

100.   ICRU(1989), *Tissue Substitutes in Radiation Dosimetry and Measurement*, in *Report 44 of the International Commission on Radiation Units and Measurements (Bethesda, MD).* p. 22.